Macrophage migration inhibitory factor regulates mitochondrial dynamics and cell growth of human cancer cell lines through CD74-NFκB signaling

Rudranil De[‡,1], Souvik Sarkar[‡,1], Somnath Mazumder[1], Subhashis Debsharma[1], Asim Azhar Siddiqui[1], Shubhra Jyoti Saha[1], Chinmoy Banerjee[1], Shiladitya Nag[1], Debanjan Saha[1], Saikat Pramanik[1] and Uday Bandyopadhyay*[,1]

[1]From the Division of Infectious Diseases and Immunology, CSIR-Indian Institute of Chemical Biology, 4, Raja S. C. Mullick Road, Jadavpur, Kolkata 700032, West Bengal, India, Tel: 91-33-24995735, Fax: 91-33-4730284.

Running title: MIF regulates mitochondrial dynamics and stability.

*To whom correspondence should be addressed: Uday Bandyopadhyay, Division of Infectious Diseases and Immunology, CSIR-Indian Institute of Chemical Biology, 4, Raja S. C. Mullick Road, Jadavpur, Kolkata 700032, West Bengal, India, Tel: 91-33-24995735, Fax: 91-33-4730284. Email: ubandyo_1964@yahoo.com, udayb@iicb.res.in

[‡] Rudranil De and Souvik Sarkar contributed equally to this work.

Abstract

The indispensable role of macrophage migration inhibitory factor (MIF) in cancer cell proliferation is unambiguous; although which specific roles the cytokine plays to block apoptosis preserving cell growth is still obscure. Using different cancer cell lines (AGS, HepG2, HCT 116 and HeLa), here we report that silencing of MIF severely deregulates mitochondrial structural dynamics by shifting the balance towards excess fission besides inducing apoptosis with increasing sub-G_0 cells. Furthermore, enhanced mitochondrial Bax translocation along with cytochrome c release, down-regulation of Bcl-xL and Bcl-2 as well as up-regulation of Bad, Bax and p53 indicate the activation of mitochondrial pathway of apoptosis upon MIF silencing. The data also indicate a concerted down-regulation of Opa1 and Mfn 1 along with a significant elevation of Drp1, cumulatively causing mitochondrial fragmentation upon MIF silencing. Upregulation of Drp1 has been found to be further coupled with fissogenic serine616 phosphorylation and serine637 dephosphorylation to ensure enhanced mitochondrial translocation. Interestingly, MIF silencing has been found to be associated with decreased NF-κB activation. In fact, NF-κB knockdown in turn increases mitochondrial fission and cell death. In addition, silencing of CD74, the cognate receptor of MIF, remarkably increases mitochondrial fragmentation besides preventing cell proliferation, inducing mitochondrial depolarization and increasing apoptotic cell death. Thus it indicates an active operation of a MIF-regulated CD74-NF-κB signaling axis for maintaining mitochondrial stability and cell growth. Collectively, we propose that MIF, through CD74, constitutively activates NF-κB to control mitochondrial dynamics and stability for promoting carcinogenesis via averting apoptosis.

Introduction

Macrophage migration inhibitory factor (MIF) is a pluripotent inflammatory marker, which is widely known for its proinflammatory role in generating immune response by activating macrophages and T cells (1). MIF has been shown to promote tumorigenesis in many models of colorectal adenomas, intestinal tumours, ovarian cancer and hepatocellular carcinoma (2-3). MIF is high in both serum and epithelial cells of gastric cancer (GC) patients (4) (5). The intricate association of upregulated MIF expression in gastro-intestinal tract malignancies makes MIF as a biomarker for gastric cancer as well as a potential target in anti-cancer therapies. In spite of its significance

in cancer, the precise role of MIF in carcinogenesis is still elusive, although, some critical MIF-mediated pathways including P115 (6), inactivation of p53 (7) and stimulation of angiogenesis (2) has been investigated. Literature also suggest that CD74, the cognate receptor of MIF, upon stimulation activates NF-κB, a key molecular player in cancer and inflammation, that triggers the entry of stimulated cells into the S phase, elevation of DNA synthesis, cell division and augmented BCL-X_L expression (8). CD74-MIF signaling is suspected to play vital prognostic role in many malignancies (9). Notably, clinical immunotherapies are also being conducted targeting CD74 by Milatuzumab, the monoclonal anti-CD74 antibody, in malignancies like B-cell lymphomas (10) and multiple myeloma (11).

Mitochondria are organelles that provide majority of the energy in most cells by synthesizing ATP (12). Being a dynamic organelle that continuously undergo fission and fusion (12), mitochondrial structural integrity plays a critical role in metabolic functions (13). Severe defects in either mitochondrial fusion or fission lead to mitochondrial dysfunction (14). Although Warburg effect proposes redundancy of mitochondrial oxidative phosphorylation as a major source of cellular bio-energy production, however the heterogeneity of cancer cell metabolism and indispensability of mitochondrial integrity to meet the bio-energetic requirements counts beyond the conventional ideology (15-16). Therefore, targeting the fine structural balance and consequent tinkering of mitochondrial integrity may force tumours to initiate death program (17-18) thereby qualifying as promising anti-neoplastic strategy.

In the present study, we propose that MIF, via CD74, maintains mitochondrial stability to favour cancer cell proliferation. We have also explored the contributing role of NF-κB in maintaining mitochondrial dynamic balance and physiological integrity to decide cell fate.

Results

MIF knockdown in gastric adenocarcinoma, hepatocellular carcinoma, cervical adenocarcinoma and colorectal carcinoma cells destabilised mitochondria, increased mitochondrial fission and reduced cell viability

MIF was knocked down in different human cancer cell lines (AGS, HepG2, HCT 116 and HeLa) by MIF-specific siRNA (siMIF) to investigate the role of MIF. Transfection efficiency was kinetically followed in AGS cells (Figure 1A) and the time point showing maximum knock down efficiency was used for further studies on cellular and sub cellular effects. Phase-contrast images for direct visualization of the AGS cells grossly indicated a significant reduction in cell density along with cyto-architectural change indicative of compromised health with prominent rounding upon MIF knockdown (Figure 1B). Data also indicated that MIF silencing drastically retarded AGS cell proliferation as evident from reduced incorporation of [^{3}H]-thymidine in the DNA of siMIF-treated cells compared to control siRNA-transfected cells as well as non-transfected cells (Figure 1C). In continuation, to assess the effect of MIF knock down on cell viability MTT reduction assay was performed wherein data indicated significantly reduced dehydrogenase activity in AGS cells conveying loss of viability (Figure 1D). We further checked the status of mitochondrial transmembrane potential, (ΔΨm), the pivotal parameter maintaining mitochondrial stability. Data revealed significant depolarization of mitochondria upon MIF silencing (Figure 1E). To assess mitochondrial functional status, we also measured total ATP content, which was found to be considerably reduced in absence of MIF in AGS cells (Figure 1F). In this scenario, we were keen to know whether MIF has any role in regulating mitochondrial structural dynamics *per se*, since loss of mitochondrial functionality and metabolic crisis is often linked with aberrant mitochondrial structure (19-20). Comparative analysis of mitochondrial morphology in control siRNA-transfected cells and MIF-silenced cells at different time points by live cell confocal microscopy revealed a significant increase in mitochondrial fission upon MIF silencing (Figure 1G) even at 24 h post transfection. Mitochondrial distribution according to the length-classification was presented with scatter plots with specific colour code corresponding to the various size ranges. Data clearly indicated that siMIF treatment significantly reduced the population of elongated mitochondrial tubules (> 4 μm) (scatter plots, Figure 1G) compared to control at 24 h which further continued to decrease with time. In addition to enhanced mitochondrial fission, significant reduction of mitochondrial mass was also clearly evident from the depletion of mitochondrial DNA (mtDNA) copy number upon siMIF treatment

compared to control siRNA treatment (Figure 1H). Collectively, the data indicated that knockdown of MIF enhanced the mitochondrial fission followed by elimination of structurally and physiologically compromised mitochondria. To check whether the mitochondrial instability triggered programmed cell death that could account for the observed loss of cell viability, flow cytometric analysis was done. Annexin V-binding confirmed apoptosis occurring at 48 h post transfection which subsequently progressed till 72 h compared to control (Figure 2A); although apoptotic changes were not significant at 24 h post transfection. This data revealed that, mitochondrial fragmentation preceded apoptosis upon MIF depletion. To check whether this enhanced mitochondrial fission is attributed to any specific cell cycle alteration, flow cytometry-based AGS cell cycle analysis was done which revealed drastic increase ($\approx$24% in siMIF-treated cells compared to 3% in control) in sub-G_0 population upon MIF knock down conveying cell death (Figure 2B). To find the link between mitochondrial structural destabilisation and induction of cell death we measured translocation of pro-apoptotic Bax to mitochondria. Immuno-confocal microscopy demonstrated enhanced mitochondrial translocation of Bax (Figure 2C) following siMIF treatment as measured by colocalization of fluorescent signals of mitochondria (red) and Bax (green) (Figure 2C). Line scan plot of merged images presented overlapping intensity peaks of enhanced Bax (green) and mitochondria (red) in MIF silenced cells (Figure 2C). To check whether the aforesaid effect of MIF silencing is specific only to gastric carcinoma cells or it is a generalised phenomenon, we used a hepatocellular carcinoma cell line, HepG2 wherein siMIF transfection was performed (Figure 3A). Data indicated reduced cell viability (Figure 3B) along with significantly depolarised mitochondria (Figure 3C) upon MIF knock down compared to control. In addition, a significant degree of mitochondrial fragmentation was observed by live cell confocal imaging in MIF-silenced HepG2 cells compared to filamentous mitochondria in cells treated with control siRNA (Figure 3D). Considerable induction of apoptosis was also observed in MIF-knocked down HepG2 cells (Figure 3E). We further checked the effect of MIF knock down in two other cancer cell lines, colorectal carcinoma cells (HCT 116) and cervical carcinoma cells (HeLa) and the data

corroborated with AGS and HepG2 cell lines, exhibiting significantly reduced viability in HeLa (Figure 4A) and HCT116 cells (Figure 4C). Comparative analysis of mitochondrial structural dynamics in MIF-silenced and control cells were evaluated in HeLa (Figure 4B) and HCT116 cells (Figure 4D) wherein enhanced mitochondrial fission upon MIF knock down was clearly evident in both cases. We next zoomed our interest in AGS cells to further explore the molecular mechanism behind the observed phenomena. To follow the status of programmed cell death machinery we checked the level of Bcl-2 family proteins and other apoptotic markers in MIF-silenced cells (Figure 5A). Data indicated significant reduction of anti-apoptotic Bcl-2 and Bcl-xL proteins concerted with elevation of pro-apoptotic Bad, Bax and cleaved caspase 3 levels (Figure 5A). Interestingly expression of p53 was also shown to be upregulated (Figure 5A). Furthermore, evaluation of cytochrome C distribution, by ELISA, revealed significant externalization from mitochondria into the cytosol which strongly indicated towards activation of intrinsic apoptosis (Figure 5B). Caspase 3 also showed remarkably increased activity upon MIF silencing (Figure 5C). Moreover, the instrumental role of intrinsic apoptosis in mediating the effects of MIF depletion was further validated by a caspase 3 inhibitor Ac-DEVD-CHO, wherein a significant reduction of apoptosis was documented when MIF depleted cells were treated with Ac-DEVD-CHO (Figure 5D). Mitochondrial stability as well as cell viability was significantly rescued by exogenous supplementation with recombinant human MIF (1 µM) (Figure 6A), proving the specificity of the proliferative action of MIF. To further validate the specificity of MIF on mitochondrial dynamics we checked mitochondrial structure in siMIF treated-MIF supplemented cells (Figure 6B). Interestingly, live cell confocal micrographs and corresponding scatter plots revealed significant retention of filamentous mitochondria in the MIF-depleted cells supplemented with exogenous MIF compared to only siMIF-treated cells (Figure 6B). Together, these data put forward evidences supporting the specific role of MIF on mitochondrial structure and cell survival.

Silencing of MIF increased the expression and mitochondrial translocation of Drp1 along with down regulation of Opa1

3

The expression and localization of mitochondrial dynamics-associated proteins were followed in control and MIF-silenced cells to confirm the induction of enhanced mitochondrial fission as observed in live cell microscopy. Mitochondrial fission is intricately associated with mitochondrial translocation of the cytosolic pro-fission mediator, dynamin-related protein 1 (Drp1) (21). Western blot analysis confirmed Drp1 elevation (Figure 7A), as well as enhanced phosphorylation at its serine616 residue (p-Drp-S616) (Figure 7A), which is essential for mitochondrial translocation. Moreover, phosphorylation at serine637 residue (p-Drp-S637), which is known to prevent mitochondrial localization, was also found to be significantly reduced in absence of MIF indicating the prevalence of a fissogenic condition (Figure 7A). High resolution confocal immunofluorescent micrographs further pinpointed enhanced mitochondrial localization of Drp1 upon siMIF treatment (Figure 7B). Line scan plot (Figure 7B) clearly indicated the differential distribution of green and red intensity peaks corresponding to mitochondria and Drp1 respectively. Distinctly separated intensity peaks were observed in control, which indicated a lesser amount of colocalization; whereas spatial overlap of the two fluorescent signals in siMIF treated cells indicated high level of colocalization (Figure 7B). Together, the data indicated that siMIF treatment enhanced mitochondrial fragmentation through elevated Drp1 import to the organelle. To validate the contribution of Drp1 in mediating MIF-depletion associated effects, Drp1 was knocked down (Figure 7C) in MIF-silenced cells and mitochondrial structure was evaluated (Figure 7D). Interestingly, significant restoration of filamentous mitochondria was observed where Drp1 was knocked down in MIF-depleted cells (Figure 7D). Distribution of mitochondrial lengths in MIF and Drp1double KD cells (scatter plot, lower right panel Figure 7D) pointed towards significant increase in filamentous mitochondrial population (> 4 μm) and lesser fragmented mitochondria (0.5 μm – 1.0 μm) compared to siMIF treatment (scatter plot, lower right panel Figure 7D). Drp1 knock down further attenuated cell death to a significant extent in MIF-silenced cells (Figure 8A) establishing the role of Drp1-dependent mitochondrial fission in MIF-silencing-induced cell death. In accord with the MTT data, flow cytometric analyses for annexin V-PI binding further confirmed the

significant reduction in apoptosis upon Drp1 KD in MIF-silenced cells (Figure 8B). Next we checked the status of mitochondrial transmembrane potential, (ΔΨm), which exhibited minor restoration in mitochondrial membrane polarization upon Drp1 silencing in absence of MIF (Figure 8C). To assess mitochondrial functional status; we measured total ATP content, which was also not found to be significantly improved upon Drp1 KD in MIF-depleted AGS cells (Figure 8D). Altogether, the data revealed that Drp1 KD could only rescue cell viability to some extent without showing major restoring effects on mitochondrial health and functionality in MIF-depleted cells. Assessment of key apoptosis mediators by immunoblotting further confirmed the anti-apoptotic effect of DRP1 silencing in MIF-KD cells as indicated from significantly diminished Bax while restored Bcl-2 level upon Drp1 KD in MIF-silenced cells (Figure 8E). Now, the absence of complete restoration of cell viability rationally directed us to check other mitochondrial structural modulators controllable by MIF. In this context, we next explored the status of mitochondrial fusion regulator proteins. Interestingly, mitochondrial fusion modulator Opa1 was found to be significantly down regulated along with decrease in Mfn1 to some extent in siMIF-treated cells compared to control siRNA treatment, as measured by densitometric analysis of the immunoblot data (Figure 8F). However, the change in level of mitochondrial fusion mediator Mfn2 was not significant (Figure 8F).

MIF regulates nuclear translocation of NF-κB for preserving filamentous mitochondria

The regulatory action of NF-κB on cell proliferation and mitochondrial health (22) next prompted us to check the effect of MIF depletion on this pivotal transcription factor. Data indicated that MIF silencing significantly blocked nuclear translocation of NF-κB in AGS cells, as evident from direct visualization by immunocytochemical imaging (Figure 9A). Confocal super resolution imaging precisely pinpointed the subcellular distribution of NF-κB (green) which was found significantly activated in the control siRNA-treated AGS cells with a clear predominance in the nucleus (blue), whereas, siMIF treatment significantly restrained NF-κB to the cytosol (Figure 9A). Moreover, ectopic supplementation with recombinant MIF in MIF-KD cells rescued NF-

4

κB activation as evident from colocalization of the signals corresponding to NF-κB and nucleus which was further quantified in terms of Pearson's correlation coefficient (Figure 9A). Altogether, the data suggested that MIF silencing abrogated NF-κB signaling. In this scenario, to check whether absence of NF-κB in the cell can produce similar effects as MIF KD, NF-κB was knocked down (Figure 9B). Data indicated that cell viability was reduced considerably upon NF-κB knock down as evident from MTT reduction assay (Figure 9C) while apoptosis was induced significantly as observed in flow cytometry (Figure 9D). Because mitochondrial fragmentation and arrested NF-κB signaling occurred as a consequence of MIF depletion, it seemed obligatory to inquire any plausible direct association of NF-κB and mitochondrial dynamics. Hence we checked the mitochondrial structure in NF-κB-silenced live cells by high resolution confocal microscopy (Figure 9E). Micrographs revealed enhanced mitochondrial fission upon NF-κB knock down in AGS cells (Figure 9E). Percent distribution of mitochondrial lengths in absence of NF-κB (scatter plots, lower right panel Figure 9E) confirmed significant reduction in filamentous mitochondrial population compared to control siRNA treatment (scatter plots, lower right panel Figure 9E). Collectively, data suggested that the knockdown of NF-κB induced mitochondrial fragmentation. Furthermore, knock down of NF-κB neutralised the rescue effect of MIF supplementation in MIF-KD cells as revealed by the flow cytometric data where significant apoptosis was detected in the MIF-supplemented cells with MIF-NF-κB double knock down (Figure 9F). In this context, to check whether restoration of cellular NF-κB level in MIF-silenced cell can ameliorate mitochondrial and cellular pathology, NF-κB was over expressed by transfecting the AGS cells with NF-κB p65 plasmid (pNF-κB p65) and parameters of mitochondrial structure and function along with cell viability were followed (Figure 10). Flow cytometric analysis revealed restored mitochondrial transmembrane potential (ΔΨm) upon NF-κB overexpression in siMIF-treated cells (Figure 10A). Moreover confocal microscopic imaging of live cells revealed the maintenance of mitochondrial filamentous population upon NF-κB overexpression in MIF-silenced cells (Figure 10B). Micrographs also revealed decreased fission of mitochondria upon

NF-κB over expression in MIF-deprived AGS cells (Figure 10B). We quantified mitochondrial length distribution (Figure 10B, lower panels). Percent distribution of mitochondrial lengths after NF-κB over expression (scatter plots, lower right panel Figure 10B) confirmed significant increase in mitochondrial filaments (> 4 μm) and reduced fragmented mitochondria (0.5 μm – 1.0 μm) compared to siMIF treatment (scatter plots, lower right panel Figure 10B). In addition, reduced apoptosis upon NF-κB over expression in MIF-deprived AGS cells (Figure 10 C) was clearly evident. Altogether the data suggested that MIF-dependent activation of NF-κB seems instrumental in AGS cell viability.

MIF-CD74 interaction is instrumental in maintaining mitochondrial structural homeostasis

As MIF is a cytokine (23), therefore we checked for any probable autocrine/paracrine mode of action that may be operating in AGS cells. A paracrine mode of action would demand externalization followed by distribution of the concerned protein on cell surface of the self as well as adjacent cells. Confocal immunofluorescence micrographs revealed that MIF was dispersed throughout the cells as well as especially on the plasma membrane (Figure 11A). Moreover, the cytozyme nature of the MIF was also evident from the tautomerase activity found in AGS cell lysate and culture media (Figure 11B) suggesting that MIF is secreted by the AGS cells. The immunoblot data further confirmed the aforesaid fact (Figure 11C). CD74 is a cognate receptor of MIF that is located on the cell surface. We assumed that MIF-CD74 interaction may be critical for all the downstream actions of MIF. To test this assumption, we treated AGS cells with anti-CD74 antibody in presence or absence of exogenously supplemented functional recombinant human MIF and followed cell proliferation by [³H]-thymidine uptake assay. Indeed the treatment with antiCD74 antibody reduced AGS cell proliferation by ~40% compared to control, a change which even exogenous MIF could not rescue (Figure 11D). To further check the effect of the absence of receptor in AGS cells, CD74 was knocked down (Figure 11E). Live cell confocal microscopy revealed significant deterioration in mitochondrial morphology in CD74-silenced cells compared to control cells (Figure 11F). Increased mitochondrial fragmentation was

5

prominently observed in CD74-silenced cells compared to tubular mitochondria in cells treated with control siRNA (Figure 11F). Mitochondrial distribution according to the length was calculated and presented with specific colour code (scatter plot, right panel Figure 11F), which pointed towards significant enhancement of fragmented mitochondrial population upon siCD74 treatment compared to control siRNA (scatter plot, left panel Figure 11F). Moreover, significant reduction in cell viability upon CD74 silencing was revealed by MTT reduction assay (Figure 11G). RNAi-dependent CD74 depletion also down regulated level of NF-κB protein to some extent in AGS cells (Figure 11H), however no significant change was observed in the mRNA level (Figure 11I). In addition pro-apoptotic Bax was found to be significantly upregulated (Figure 11H). Moreover, cellular ATP level was also found to be severally reduced (Figure 11J) and mitochondria were found to be significantly depolarised (Figure 11K) along with increased apoptosis (Figure 11L) upon CD74 KD. Collectively, the data indicated that selective knockdown of CD74 induced pronounced deterioration of mitochondrial function and morphological integrity to induce apoptosis.

Discussion

In this study, we report the essential role of MIF in maintaining mitochondrial dynamics and stability in cancer cells to promote proliferation. We also provide evidence that MIF, through CD74, constitutively activates NF-κB, which in turn control mitochondrial fission-fusion balance to decide mitochondrial structural and functional stability.

Most cancer cells including human gastric adenocarcinoma (AGS) cells inherently produce very high level of MIF (24). We evaluated mitochondrial morphology and cell proliferation of AGS, HepG2, HeLa and HCT 116 cells after silencing MIF to check whether the observed effects are common in cancer. Mitochondrial instability is detrimental because it can trigger intrinsic pathway of apoptosis. Therefore, cancer cells deploy a strict surveilling arsenal of cytoprotective proteins to tightly regulate mitochondrial integrity and fission-fusion balance for levying apoptotic block to ensure sustained proliferation. Thus targeting mitochondrial dynamics of cancer cell can unveil novel anti-neoplastic strategies. In the aforesaid context, to elucidate the plausible regulatory action of MIF on maintaining mitochondrial structural dynamic balance, we monitored mitochondrial functional and structural alterations upon MIF knockdown.

Healthy mitochondria supply energy, perform metabolic regulation and control redox homeostasis. In cancer cells, mitochondria are among the primary concerns due to their lethal capacity to activate apoptosis. Because, retardation of cell proliferation along with loss of cell viability was evident upon MIF knock down, we were interested to assess mitochondrial stability in absence of MIF. In this context, significant mitochondrial depolarisation coupled with reduced ATP production pointed towards compromised electron transport chain functionality. Mitochondrial fragmentation often occurs as a result of inner membrane depolarisation and *vice versa* (25). Mitochondrial structure and function maintain the balance between anti- and pro-apoptotic signaling in most cells (26) determining the sensitivity to anti-neoplastic drugs like cisplatin and staurosporine in cancer cells (27-28). Aberrant mitochondrial fission is often intricately associated with mitochondrial pathology (29-30) which can trigger apoptosis. Hence, we were keen to know, whether MIF plays any role in maintaining mitochondrial dynamic equilibrium. Real time visualisation of mitochondrial structure in live cells followed by morphometric analysis showed that absence of MIF interferes with the maintenance of mitochondrial dynamics by shifting the balance towards excess fission. Kinetic analysis of mitochondrial fragmentation in relation to apoptosis suggested that indeed mitochondrial fragmentation preceded apoptosis during MIF knock down thereby sensitizing the cells to progressively die at the advanced hours of transfection when the cells severely lack MIF. Notably, mitochondrial fission is also a physiological process that actively operates during cell division for mitochondrial segregation into the resultant daughter cells. Therefore, to check whether the observed fission was a characteristic event taking place during any specific stage of the cell cycle in siMIF-treated cells, we analysed cell cycle in absence of MIF. No significant alteration in cell cycle was observed upon siMIF transfection, however, increase in the sub-G_0 population clearly indicated towards enhanced cell death upon MIF silencing. Interestingly enhanced fission was found to be positively associated with significant

compromise in mitochondrial health and functionality as evident from membrane depolarization and ATP formation leading to cellular bio-energetic crisis. Functionally compromised mitochondria are normally eliminated from the cell (31-32) leading to a partial reduction in mitochondrial mass (33). siMIF-induced reduction in mtDNA copy number is therefore a prominent proof of enhanced clearance of the functionally compromised mitochondria, further justifying the radical depletion in ATP upon MIF silencing. Excess mitochondrial fission coupled with elevated clearance and ensuing bio-energetic crisis is generally associated with mitochondrial recruitment of the mitochondrial permeability transition pore (MPTP)-forming Bax to initiate cell death via cytochrome C release into the cytosol (34-35) for apoptosome formation. In the aforesaid context, it is worth mentioning that MIF knock down-associated hyperfission was positively linked with enhanced Bax translocation to mitochondria along with concomitant externalisation of cytochrome C. Interestingly, the instrumental role of caspase 3 and hence intrinsic apoptosis in mediating MIF-depletion associated apoptotic sensitization was further confirmed from the responsiveness to specific caspase 3 inhibitor. Furthermore, the rescue effect of exogenous MIF supplementation, in a MIF-KD background, on mitochondrial dynamics and apoptosis validated the obligatory role of MIF in maintaining mitochondrial integrity and associated cell viability. Because mitochondrial fragmentation proceeds with sequential post translational modification of fissogenic GTPase Drp1 conducive for allowing mitochondrial translocation, the observation of Drp1 serine^{616} and serine^{637} phosphorylations upon MIF knock down clearly indicated towards the operation of Drp1-depedent fission as the predominant fissogenic event in the present study. However, it is noteworthy that Drp1-knock down was not sufficient to restore complete metabolic integrity (by rescuing siMIF-induced mitochondrial membrane depolarization and ATP depletion), although significant protection against apoptosis was successfully conferred to retain viability. A logical explanation to this apparent discrepancy is that, though prevention of mitochondrial structural instability might have interfered with aggravating apoptotic sensitization due to loss of MIF, it failed to preserve metabolic integrity which might be regulated by a complex interplay

of myriad subcellular and micro-environmental factors. Moreover, the apparently enhanced responsiveness of Bcl-2 over Bcl-xL due to Drp1 knock down, in MIF-depleted cells, further pointed towards the differential interplay of Bcl-2 family proteins in a condition-specific manner. In addition to fissogenic mediators, mitochondrial dynamics and hence physiological integrity is under strict regulation of fusogenic mediators as well (19). In this regard MIF-depletion associated pro-fission signaling is further potentiated by reduced expression of fusion mediators including Optic atrophy 1 protein (Opa1) and Mitofusin 1 (Mfn1) to some extent, thereby implying a synergistic effect of both fission and fusion mediators in eliciting mitochondrial structural destabilization. Hence, it can be safely postulated that, selective knockdown of MIF causes AGS cell lethality by incurring mitochondrial pathology.

CD74 is a cognate receptor of MIF that is located on the cell surface. The intracellular domain (ICD) of CD74, upon MIF-CD74 interaction, undergoes proteolytic processing to activate several downstream signaling pathways, which ultimately lead to cell proliferation. CD74/MIF interaction-mediated molecular signal transduction often involves the nuclear translocation of the key transcription factor NF-κB (36-38) that orchestrate anti-apoptotic responses in both cancer (39) and normal cells (40). Several molecular pathways linked with NF-κB and mitochondria have been investigated for the possible cause of apoptosis or growth retardation (5,7) however, the exact mechanism is still elusive. To this end, the present study highlights the regulation of NF-κB activation via CD74/MIF pathway. Recent studies also indicate that NF-κB controls mitochondrial dynamics (22) along with many BCL-2 family proteins important for maintaining cell viability (41). It is established that, NF-κB activation during cell proliferation is associated with preservation of mitochondrial integrity (42-43). Recently, it has been also shown that NF-κB-signaling has direct impact on mitochondrial network and expression of OPA1, the inner mitochondrial membrane pro-fusion GTPase responsible for cristae remodelling (22) and hence proper retention of cytochrome C within mitochondria (44) (45). In this regard, we inquired the role of NF-κB signaling in the MIF-mediated apoptotic block and found a prominent inhibition of NF-κB signaling, upon treatment with siMIF, via restricted activation and nuclear translocation of

this transcription factor, thereby collapsing the pro-survival network. Notably, treatment with siRNA specific to NF-κB was also found to be positively associated with mitochondrial fragmentation and associated depletion in cellular viability thereby triggering apoptosis. In addition NF-κB-KD also neutralised the rescue effect of recombinant MIF supplementation. Interestingly, overexpression of NF-κB in MIF-depleted cells and consequent restoration of mitochondrial structural and functional homeostasis and cell viability confirmed the quintessential role of NF-κB and mitochondrial dynamic balance in maintaining MIF-dependent cancer cell integrity.

Detection of MIF on the plasma membrane as well as within the AGS cells highlighted the existence of this active cytozyme which was further reiterated from its presence in the cell lysate and culture medium indicating the autocrine and paracrine nature respectively. MIF transduces most of its biomolecular signals upon interaction with its transmembrane receptor CD74 (46) apart from interactions with other receptors like CD44, CXCR2, CXCR4 or CXCR7. In the aforesaid context, we were very curious to know the fate of AGS cells after blocking the signal initiation by interfering with MIF-CD74 interaction as well as CD74 depletion. Interestingly, anti-CD74 antibody-induced retardation of cell growth closely corroborated with the data exhibiting loss in cell viability upon CD74 knock down. Notably, CD74 knock down exhibited similar effect as MIF-silencing on mitochondrial integrity, bioenergetic status and cellular viability inducing increased fission and apoptosis as evident from increase in Bax which further justified the flow cytometry-based evidence of apoptosis. Pro-survival NF-κB, which is constitutively activated in cancer cells was found to be reduced to some extent upon CD74 knock down, however not much change in transcript level could be documented. It may be presumed that owing to the multiple regulatory actions of NF-κB in diverse cellular processes (47), its expression is tightly regulated (48-49). However the decrease in protein level is probably due to MIF-depletion associated restricted cell proliferation along with no transcriptional upregulation/compensation during advanced apoptosis. Taken together, these observations confirm the active operation of CD74-MIF crosstalk to ensure cancer cell viability by maintaining mitochondrial dynamic integrity.

In conclusion, we propose that MIF, which is endogenously over expressed in AGS cells, acts as a critical regulator of mitochondrial fission-fusion dynamics and health to sustain cell proliferation by imparting apoptotic-block via interaction with CD74 and consequent NF-κB activation. Thus, disruption of MIF-induced pro-survival signaling by targeting mitochondrial dynamics might serve as a potent non-canonical anti-neoplastic therapeutic target against gastric carcinoma.

Experimental procedures

Materials

MTT, phosphatase inhibitor cocktail and paraformaldehyde were obtained from Sigma. Fetal bovine serum, mitotracker red, JC-1, Alexa Fluor 647, Alexa Fluor 488 and Oregon green 488 tagged antibodies, ATP Determination Kit, Optimem, Lipofectamine RNAiMAX were procured from Life technologies. MIF siRNA (cat# sc-37137), Drp1 siRNA (cat# sc-43732), CD74 siRNA (cat# sc-35023), NF-κB (p65) siRNA (cat# sc-29410) control siRNA (cat# sc-37007), antibodies specific for Bcl-2 (cat# sc-7382), Bax (cat# sc-7480), TOM20 (cat# sc-136211), CD74 (cat# sc-5438), Bcl-xL (cat# sc-8392, cat# 2764T), were procured from santacruz biotechnology. MIF (cat# ab175189). CD-74 (cat# ab9514), NF-κB (p65) (cat# ab7970), Drp-1 (cat# ab54038), Mfn1 (cat# ab57602), Mfn2 (cat# ab56889) antibodies were procured from Abcam. Actin antibody was obtained from Biovision (cat# 3598R-100). Antibodies to Bad (cat# 9292S), cleaved Caspase 3 (cat# 9664s), p53 (cat# 9282s), p-Drp-S616 (cat# 3455s) and p-Drp-S637 (cat# 4867s) were purchased from Cell signaling technology. pNF-κB p65 (over expression plasmid) was purchased from Addgene. Protease inhibitor cocktail was purchased from calbiochem. F-12 Ham Kaighn's Modification media and Dulbecco modified Eagle medium were procured from Hi-Media Laboratories. All other reagents were of analytical grade purity.

Human gastric adenocarcinoma, hepatocellular carcinoma, cervical adenocarcinoma and colorectal carcinoma cell culture

AGS cells (human gastric epithelial cells) (ATCC-CRL-1739) and HepG2 (human hepatocellular carcinoma cells (ATCC-HB-

8065) were obtained from American Type Culture Collection (Manassas, USA). AGS and HepG2 were cultured in nutrient mixture F-12 Ham, Kaighn's modification and Dulbecco modified Eagle medium (DMEM), respectively, supplemented with 10% FBS. HCT 116 (human colorectal carcinoma) and HeLa (human cervical adenocarcinoma) cells were cultured in DMEM supplemented with 10% FBS. All cell culture media were supplemented with 100 units/mL penicillin, 100 µg/mL streptomycin and 10 µg/mL gentamycin. The cells were maintained at 37 °C in 5% CO_2 incubator. The cells were split by trypsinization in 1X trypsin-EDTA solution once every 3 days. For all the experiments, cells between passage numbers 5 to 10 were used. For immunofluorescence studies cells were grown on poly lysine coated glass cover-slips or glass bottom culture dishes.

siRNA and other treatments in AGS, HepG2, HCT 116 and HeLa cell lines

Transfection with MIF, Drp1, NF-κB and CD74 siRNAs (siMIF, siDrp1, siNF-κB and siCD74) were performed according to the manufacturer's protocol. Briefly, 80 pM siRNA and lipofectamine suspended in optimem was used for each transfection. After transfection, the cells were incubated overnight. Next day, media was replaced by complete cell culture media and cells were maintained for 72h. Different incubations (24 h and 48 h) were done to check time dependent knockdown and transfection efficiency. Transfections with scrambled siRNAs (control siRNA) were performed each time. Cells were harvested at 72h post transfection and processed for subsequent assays (in case of siMIF, siNF-κB and siCD74) and at 48h post transfection (in case of siDrp1). The sequences of siRNAs used are as follows, where all sequences are provided in 5′ → 3′ orientation, -: MIF siRNA (sc-37137) is a pool of 3 different siRNA duplexes; sc-37137A: sense: GACAGGGUCUACAUCAACUtt and antisense: AGUUGAUGUAGACCCUGUCtt; sc-37137B: sense: CAGGGUCUACAUCAACUAUtt and antisense: AUAGUUGAUGUAGACCCUGtt; sc-37137C: sense: GAGAAAUAAACGGUUUAGAtt and antisense: UCUAAACCGUUUAUUUCUCtt. The sequence of DRP1 siRNA (sc-43732) is sense: AACGCAGAGCAGCGGAAAGAGtt and antisense: CUCUUUCCGCUGCUCUGCGUUtt. CD74

siRNA (sc-35023) is a pool of 3 different siRNA duplexes; sc-35023A: sense: CCCAAGCCUGUGAGCAAGAtt and antisense: UCUUGCUCACAGGCUUGGGtt; sc-35023B: sense: GAGAGCUGGAUGCACCAUUtt and antisense: AAUGGUGCAUCCAGCUCUCtt; sc-35023C: sense: CUGACGCUCCACCGAAAGAtt and antisense: UCUUUCGGUGGAGCGUCAGtt. The sequence of: NFκB p65 siRNA (sc-29410) is: sense: GCCCUAUCCCUUUACGUCtt and antisense: GACGUAAAGGGAUAGGGCtt. Over expression of NF-κB was achieved by lipofectamine-mediated transfection of NF-κB p65 plasmid (pNF-κB p65). In caspase 3 inhibition assay the caspase 3 inhibitor Ac-DEVD-CHO (20 µM) was added 30 min before siRNA treatment (50).

Immunoblot analysis

AGS cells were lysed in the cell lysis buffer supplemented with the protease inhibitor cocktail and subsequently centrifuged. The supernatant was quantified by Lowry method (51) and 50 µg protein was resolved in 10% SDS page at constant voltage (100 V) for immunoblotting. Pre-stained standards were used as molecular weight markers and were run in parallel. Proteins were then transferred to a nitrocellulose membrane by wet transfer method with a current intensity of 400 mA for 75 min in a 190 mM glycine, 20 mM Tris base buffer (pH 8.3) containing 20% methanol. The membrane was incubated for 1 h in 5% nonfat dry milk blocking buffer in TBS (25 mM Tris, 150 mM NaCl, 2 mM KCl, pH 7.4). The membrane was incubated over-night at 4°C with the following antibodies: anti-MIF (dilution 1:1000), anti-β-actin (dilution 1: 2000), anti-Bcl-2 (dilution 1:500), anti-Bcl-xL (dilution 1: 1000), anti-Bax (dilution 1:400), anti-Bad (dilution 1:1000), anti-cleaved Caspase 3 (dilution 1: 1000), anti-p53 (dilution 1: 1000), anti-Drp1 (dilution 1: 1000 for abcam, 1:500 for santacruz biotechnology), anti-p-Drp-S616 (dilution 1: 1000) and anti-p-Drp-S637 (dilution 1: 1000), anti-Opa1 (dilution 1: 1000), anti-Mfn1 (dilution 1: 1000), anti-Mfn2 (dilution 1: 1000), anti-CD74 (dilution 1: 1000), anti-NF-κB (dilution 1: 1000). After washing with TBS solution containing 0.1% Tween 20 (TBS-T buffer), the membrane was incubated for 2h in secondary antibody solution (1:2000 HRP-labeled anti-rabbit or anti-mouse IgG). Subsequently the membrane was washed

9

with TBS-T buffer and the protein bands were detected either by imaging in Biorad Chemidoc MP System or by scanning the developed blots in HP Laser Jet M1005 MFP Scanner. The densitometric analysis of the detected bands was performed in ImageJ software.

[³H]-thymidine incorporation to follow cell proliferation

AGS cells (1×10^4 cells/ mL) were seeded in triplicates for each set in 96 well plates and allowed to grow for 36 hours. Thereafter, transfection was done and kept for another 48 hours after which [³H]-thymidine (5 μCi) was added and again incubated for 24h. Finally the cells were harvested and transferred to scintillation liquid. For CD74 neutralization experiment, cells were incubated with anti-CD74 antibody (52) and [³H]-thymidine was added after 24h of incubation. After 24 hr radioactive counts were taken in a scintillation counter (Tricarb 2810TR, PerkinElmer) and expressed as disintegrations/min.

Cell viability assessment by MTT reduction

Mitochondrial dehydrogenase activity was measured by 3-(4,5-dimethylthiazol-2-yl)-2,5-diphenyl tetrazolium bromide (MTT) reduction assay. Briefly, cells after treatments were incubated with MTT (0.1% final concentration) in PBS for 4h at 37 ^{0}C/ 5% CO_2 condition. The purple formazan was dissolved in anhydrous DMSO and was measured at 570 nm in spectrophotometric plate reader (BioTek).

Measurement of mitochondrial trans-membrane potential (ΔΨm)

ΔΨm was measured by 5,5′,6,6′-tetrachloro-1,1′,3,3′-tetraethylbenzimidazolylcarbocyanine iodide dye (JC-1), according to manufacturer's protocol. Briefly, equal amount of AGS cells (1×10^6), after treatment, were rinsed in pre-warmed phosphate-buffered saline (PBS) and incubated in warm PBS containing JC-1 (2 μM final concentration) for 15 min at 37°C in 5% CO_2 in darkness. The cells were next pelleted and resuspended in PBS and analyzed by fluorescence-activated cell sorter (FACS) LSR Fortessa. Data were analyzed using FACS DIVA software.

Measurement of ATP content

ATP was measured using ATP determination kit (Invitrogen Corp., Carlsbad, CA, USA) by following manufacturer's instructions. In brief,

cells after treatment were lysed in cell lysis buffer and clear supernatant was used for the measurement of ATP in a luminometer (BioTek) as relative light unit (RLU) after subtracting blank. The values were normalized by protein concentrations of the respective samples.

Confocal and super resolution STED microscopy

For live cell confocal microscopy, to evaluate mitochondrial fragmentation, cells plated on glass bottom dish were washed with pre-warmed media after the treatment and loaded with MitoTracker Red (100 nM, diluted in warm media) for 20 minutes at 37°C in a CO_2 incubator. The cells were subsequently washed thrice in warm media and viewed under 63X oil immersion lens of the Leica TCS-SP8 confocal microscope provided with a thermo-regulated stage in 5% CO_2 environment. Quantification of mitochondrial length was done with necessary thresholding in "LAS-X" software taking entire micrographs. Approximately 100 cells were scanned and the experiments were performed thrice. The laser intensities were kept <2% throughout and image acquisition time were kept as low as possible to avoid any possible laser-induced toxicity.

In case of immunofluorescence experiments, AGS cells, plated on poly lysine coated cover-slips, were washed with pre-warmed media after the treatment and loaded with mito-tracker-red followed by fixation with 3% paraformaldehyde and permeabilization in 0.15% triton-x-100. Cells were next washed and blocked in 2% BSA in PBS. For measuring Bax translocation, immunostaining was done using anti-Bax primary and Alexa Fluor 488-conjugated secondary antibodies. In case of Drp-1 localization, mitochondria were stained with anti TOM20 primary (1:100) and Alexa Fluor 488-conjugated secondary antibodies while Drp1 immunostaining was done by anti-Drp-1 primary (1:500) and Alexa Fluor 647-conjugated secondary antibodies. MIF immunostaining was done by anti-MIF (1:250) primary and Alexa Fluor 647-conjugated secondary antibodies (1:1000) for checking MIF expression. Leica TCS-SP8 confocal microscope was used for visualization. Anti-NF-κB (1:400) primary and Oregon green 488-conjugated secondary antibodies (1:500) along with DAPI (to stain nucleus) was used for studying detect nuclear translocation of NF-κB. Nucleus was viewed in a separate channel to avoid overlapping of the

10

emission spectra. For precise analysis of intracellular NF-κB distribution, STED super resolution microscopy was used wherein the samples were imaged under 100X oil immersion objective lens by a 592 nm depletion laser. Z-stacking was done during image capture and morphometric analysis was done after binary thresholding. Digital zooming was performed as required. Images were cropped and processed globally using Adobe Photoshop CS6. Images were assembled in CorelDRAW X7 software to prepare the figure.

RNA isolation and real-time RT-PCR

Total RNA was isolated from control and experimental sets using TRIzol method as manufacturer's protocol. Plausible DNA contamination was removed by treatment with rDNase (Ambion) as per the manufacturer's instructions and the resultant pure RNA was spectrophotometrically measured. Subsequently 2 μg of RNA was used for cDNA preparation using RevertAid First Strand cDNA synthesis kit (Thermo Fisher Scientific Inc.). The obtained cDNA were diluted and used for qPCR reaction as mentioned previously (33) with primers against *NF-κB* and *GAPDH*. The primer sequences were as follows,- *NF-κB* Forward : 5′-CCAGACCAACAACAACCCCT-3′, reverse: 5′-TCACTCGGCAGATCTTGAGC-3′. *GAPDH* Forward: 5′- AGTATGACTCTACCCACGGC -3′, reverse: 5′-TGAAGACGCCAGTAGACTCC-3′. The gene expression profile was calculated by $2^{-\Delta\Delta cq}$ analysis and expressed as fold change relative to control after normalization with *GAPDH*.

Analysis of mitochondrial copy number

Mitochondrial content was assessed by calculating the ratio of mtDNA and nuclear DNA as mentioned previously (33) with minor modifications. Briefly control siRNA and siMIF treated cells were subjected to DNA isolation using DNA isolation kit (Qiagen). Subsequently qPCR-based amplification of nuclear and mitochondrial DNA was performed using primers specific for nucleus-encoded and mitochondria-encoded genes respectively. The ratio of the resultant $2^{-\Delta\Delta cq}$ values corresponding to mitochondrial and nuclear gene was used for estimation of mitochondrial copy number. The primer sequences used in the qPCR reaction are as follows: Nuclear DNA segment, forward: 5′-TGCTGTCTCCATGTTTGATGTATCT-3′, reverse: 5′- TCTCTGCTCCCCACCTCTAAGT-

3′; mitochondrial DNA segment 1: forward: 5′-CACCCAAGAACAGGGTTTGT-3′, reverse: 5′-TGGCCATGGGTATGTTGTTA-3′; mitochondrial DNA segment 2: forward: 5′-CCCTAACACCAGCCTAACCA-3′, reverse: 5′-AAAGTGCATACCGCCAAAAG-3′; Calculations were normalised with Nuclear Hbb gene amplified using forward: 5′-CTATGGGACGCTTGATGT-3′ and reverse: 5′-GCAATCATTCGTCTGTTT-3′ primers.

Cell cycle analysis

Cell cycle analysis was performed by flow cytometric analysis. AGS cells were first harvested and fixed in chilled ethanol (70% v/v) overnight at 4°C. Fixed cells were stained in PBS containing 100 μg/ml propidium iodide (P-4170, Sigma) and 20 μg/ml RNase A (# 12091-039, Invitrogen) followed by analysis in BD LSR Fortessa using BD FACS Diva 6.2 software.

FITC-annexin V staining for cell death determination

Apoptosis in the AGS cells was measured by annexin V/ propidium iodide (PI) dual staining. Briefly, after treatment the media was discarded and the cells were harvested by trypsinization and counted. 1×10^6 cells were taken and stained with FITC-annexin V in annexin V binding buffer (Abcam) following the manufacturer's protocol. The cells were next counterstained with PI and finally analyzed in FACS LSR Fortessa, BD, with FITC signal detector and phycoerythrin (PE) signal detector using FACS DIVA software under standard parameters.

Measurement of cytochrome c content

Cytosolic fraction was isolated by Mitochondria Isolation Kit (Thermo Fisher Scientific Inc., USA) and the cytosolic (non-mitochondrial fraction) Cytochrome C level was estimated by Cytochrome C ELISA kit (Quantikine ELISA, R&D systems) according to the manufacturer's protocol.

Assay of caspase-3 activity

Caspase activity assay was performed using commercially available Caspase 3 assay kit (Calbiochem; Merck, Germany) following manufacturer's protocol. Briefly, cells after treatment were lysed in a buffer without protease inhibitor cocktail. Subsequently protein estimation was done and equal amount of protein

was used for Caspase 3 activity assay. The mixture was incubated at 37 ℃ for 2 hr; and fluorescence was measured at 505 nm.

Cloning, over-expression and purification of human MIF

Human MIF was cloned, over expressed and purified as mentioned earlier and the identity was further confirmed by MALDI-TOF mass analysis and peptide finger printing (37).

Assay of tautomerase activity of MIF

Tautomerase activity of MIF was determined as described earlier (37). Briefly, the activity was determined at 25 ℃ by adding L-DOPA (0.25–1.5mM) to AGS cell lysate in 10 mM potassium phosphate buffer, pH 6.2 containing 0.5 mM EDTA or AGS cell culture media and

conversion of L-DOPA (coloured) to indole carboxylic acid methyl ester (colourless) was measured at 475 nm.

Statistical analysis

All experiments were performed in triplicates and repeated. Statistical analyses of the data were done in GraphPad Prism 6.0 and the data were expressed as mean ± SEM (standard error of mean). Calculations of the level of significance (P) were done by unpaired 't test' where the number of samples were two and by ANOVA (followed by Bonferroni's post hoc analysis) where the experimental sets exceeded two. P value less than 0.05 ($P < 0.05$) was considered statistically significant.

Conflict of interest

The authors declare that they have no conflicts of interest with the contents of this article.

References

1. Baumann, R., Casaulta, C., Simon, D., Conus, S., Yousefi, S., and Simon, H. U. (2003) Macrophage migration inhibitory factor delays apoptosis in neutrophils by inhibiting the mitochondria-dependent death pathway. *FASEB journal : official publication of the Federation of American Societies for Experimental Biology* **17**, 2221-2230

2. Wilson, J. M., Coletta, P. L., Cuthbert, R. J., Scott, N., MacLennan, K., Hawcroft, G., Leng, L., Lubetsky, J. B., Jin, K. K., Lolis, E., Medina, F., Brieva, J. A., Poulsom, R., Markham, A. F., Bucala, R., and Hull, M. A. (2005) Macrophage migration inhibitory factor promotes intestinal tumorigenesis. *Gastroenterology* **129**, 1485-1503

3. Hira, E., Ono, T., Dhar, D. K., El-Assal, O. N., Hishikawa, Y., Yamanoi, A., and Nagasue, N. (2005) Overexpression of macrophage migration inhibitory factor induces angiogenesis and deteriorates prognosis after radical resection for hepatocellular carcinoma. *Cancer* **103**, 588-598

4.   Morris, K. T., Nofchissey, R. A., Pinchuk, I. V., and Beswick, E. J. (2014) Chronic macrophage migration inhibitory factor exposure induces mesenchymal epithelial transition and promotes gastric and colon cancers. *PloS one* **9**, e98656

5.   Shimwell, N. J., Ward, D. G., Mohri, Y., Mohri, T., Pallan, L., Teng, M., Miki, Y. C., Kusunoki, M., Tucker, O., Wei, W., Morse, J., and Johnson, P. J. (2012) Macrophage migration inhibitory factor and DJ-1 in gastric cancer: differences between high-incidence and low-incidence areas. *British journal of cancer* **107**, 1595-1601

6.   Li, X. J., Luo, Y., and Yi, Y. F. (2013) P115 promotes growth of gastric cancer through interaction with macrophage migration inhibitory factor. *World journal of gastroenterology* **19**, 8619-8629

7.   Hudson, J. D., Shoaibi, M. A., Maestro, R., Carnero, A., Hannon, G. J., and Beach, D. H. (1999) A proinflammatory cytokine inhibits p53 tumor suppressor activity. *The Journal of experimental medicine* **190**, 1375-1382

8.   Starlets, D., Gore, Y., Binsky, I., Haran, M., Harpaz, N., Shvidel, L., Becker-Herman, S., Berrebi, A., and Shachar, I. (2006) Cell-surface CD74 initiates a signaling cascade leading to cell proliferation and survival. *Blood* **107**, 4807-4816

9.   Kindt, N., Lechien, J. R., Nonclercq, D., Laurent, G., and Saussez, S. (2014) Involvement of CD74 in head and neck squamous cell carcinomas. *Journal of cancer research and clinical oncology* **140**, 937-947

10.   Martin, P., Furman, R. R., Rutherford, S., Ruan, J., Ely, S., Greenberg, J., Coleman, M., Goldsmith, S. J., and Leonard, J. P. (2015) Phase I study of the anti-CD74 monoclonal antibody milatuzumab (hLL1) in patients with previously treated B-cell lymphomas. *Leukemia & lymphoma* **56**, 3065-3070

11.   Kaufman, J. L., Niesvizky, R., Stadtmauer, E. A., Chanan-Khan, A., Siegel, D., Horne, H., Wegener, W. A., and Goldenberg, D. M. (2013) Phase I, multicentre, dose-escalation trial of monotherapy with milatuzumab (humanized anti-CD74 monoclonal antibody) in relapsed or refractory multiple myeloma. *British journal of haematology* **163**, 478-486

12.   Zhao, J., Zhang, J., Yu, M., Xie, Y., Huang, Y., Wolff, D. W., Abel, P. W., and Tu, Y. (2013) Mitochondrial dynamics regulates migration and invasion of breast cancer cells. *Oncogene* **32**, 4814-4824

13.   Westermann, B. (2010) Mitochondrial fusion and fission in cell life and death. *Nature reviews. Molecular cell biology* **11**, 872-884

14.   Amati-Bonneau, P., Valentino, M. L., Reynier, P., Gallardo, M. E., Bornstein, B., Boissiere, A., Campos, Y., Rivera, H., de la Aleja, J. G., Carroccia, R., Iommarini, L., Labauge, P., Figarella-Branger, D., Marcorelles, P., Furby, A., Beauvais, K., Letournel, F., Liguori, R., La Morgia, C., Montagna, P., Liguori, M., Zanna, C., Rugolo, M., Cossarizza, A., Wissinger, B., Verny, C., Schwarzenbacher, R., Martin, M. A., Arenas, J., Ayuso, C., Garesse, R., Lenaers, G., Bonneau, D., and Carelli, V. (2008) OPA1 mutations induce mitochondrial DNA instability and optic atrophy 'plus' phenotypes. *Brain : a journal of neurology* **131**, 338-351

15.   Jezierska-Drutel, A., Rosenzweig, S. A., and Neumann, C. A. (2013) Role of oxidative stress and the microenvironment in breast cancer development and progression. *Advances in cancer research* **119**, 107-125

16.   Chen, H., and Chan, D. C. (2017) Mitochondrial Dynamics in Regulating the Unique Phenotypes of Cancer and Stem Cells. *Cell metabolism* **26**, 39-48

17.   Alirol, E., and Martinou, J. C. (2006) Mitochondria and cancer: is there a morphological connection? *Oncogene* **25**, 4706-4716

18.   Panngom, K., Baik, K. Y., Nam, M. K., Han, J. H., Rhim, H., and Choi, E. H. (2013) Preferential killing of human lung cancer cell lines with mitochondrial dysfunction by nonthermal dielectric barrier discharge plasma. *Cell death & disease* **4**, e642

19.   Galloway, C. A., and Yoon, Y. (2013) Mitochondrial morphology in metabolic diseases. *Antioxid Redox Signal* **19**, 415-430

20.   Schrepfer, E., and Scorrano, L. (2016) Mitofusins, from Mitochondria to Metabolism. *Mol Cell* **61**, 683-694

21.   Fischer, T. D., Hylin, M. J., Zhao, J., Moore, A. N., Waxham, M. N., and Dash, P. K. (2016) Altered Mitochondrial Dynamics and TBI Pathophysiology. *Frontiers in systems neuroscience* **10**, 29

22.   Laforge, M., Rodrigues, V., Silvestre, R., Gautier, C., Weil, R., Corti, O., and Estaquier, J. (2016) NF-kappaB pathway controls mitochondrial dynamics. *Cell Death Differ* **23**, 89-98

23.   Kasama, T., Ohtsuka, K., Sato, M., Takahashi, R., Wakabayashi, K., and Kobayashi, K. (2010) Macrophage migration inhibitory factor: a multifunctional cytokine in rheumatic diseases. *Arthritis* **2010**, 106202

24. He, L. J., Xie, D., Hu, P. J., Liao, Y. J., Deng, H. X., Kung, H. F., and Zhu, S. L. (2015) Macrophage migration inhibitory factor as a potential prognostic factor in gastric cancer. *World journal of gastroenterology* **21**, 9916-9926

25. de Arriba, G., Calvino, M., Benito, S., and Parra, T. (2013) Cyclosporine A-induced apoptosis in renal tubular cells is related to oxidative damage and mitochondrial fission. *Toxicology letters* **218**, 30-38

26. Parsons, M. J., and Green, D. R. (2010) Mitochondria in cell death. *Essays in biochemistry* **47**, 99-114

27. Frank, S., Gaume, B., Bergmann-Leitner, E. S., Leitner, W. W., Robert, E. G., Catez, F., Smith, C. L., and Youle, R. J. (2001) The role of dynamin-related protein 1, a mediator of mitochondrial fission, in apoptosis. *Developmental cell* **1**, 515-525

28. Fan, S., Liu, B., Sun, L., Lv, X. B., Lin, Z., Chen, W., Chen, W., Tang, Q., Wang, Y., Su, Y., Jin, S., Zhang, D., Zhong, J., Li, Y., Wen, B., Zhang, Z., Yang, P., Zhou, B., Liang, Q., Yu, X., Zhu, Y., Hu, P., Chu, J., Huang, W., Feng, Y., Peng, H., Huang, Q., Song, E., and Li, J. (2015) Mitochondrial fission determines cisplatin sensitivity in tongue squamous cell carcinoma through the BRCA1-miR-593-5p-MFF axis. *Oncotarget* **6**, 14885-14904

29. Bossy-Wetzel, E., Barsoum, M. J., Godzik, A., Schwarzenbacher, R., and Lipton, S. A. (2003) Mitochondrial fission in apoptosis, neurodegeneration and aging. *Current opinion in cell biology* **15**, 706-716

30. Wai, T., and Langer, T. (2016) Mitochondrial Dynamics and Metabolic Regulation. *Trends in endocrinology and metabolism: TEM* **27**, 105-117

31. Kotiadis, V. N., Duchen, M. R., and Osellame, L. D. (2014) Mitochondrial quality control and communications with the nucleus are important in maintaining mitochondrial function and cell health. *Biochim Biophys Acta* **1840**, 1254-1265

32. Herst, P. M., Rowe, M. R., Carson, G. M., and Berridge, M. V. (2017) Functional Mitochondria in Health and Disease. *Front Endocrinol (Lausanne)* **8**, 296

33. De, R., Mazumder, S., Sarkar, S., Debsharma, S., Siddiqui, A. A., Saha, S. J., Banerjee, C., Nag, S., Saha, D., and Bandyopadhyay, U. (2017) Acute mental stress induces mitochondrial bioenergetic crisis and hyper-fission along with aberrant mitophagy in the gut mucosa in rodent model of stress-related mucosal disease. *Free radical biology & medicine* **113**, 424-438

34. Youle, R. J., and Karbowski, M. (2005) Mitochondrial fission in apoptosis. *Nature reviews. Molecular cell biology* **6**, 657-663

35. Karbowski, M., Lee, Y. J., Gaume, B., Jeong, S. Y., Frank, S., Nechushtan, A., Santel, A., Fuller, M., Smith, C. L., and Youle, R. J. (2002) Spatial and temporal association of Bax with mitochondrial fission sites, Drp1, and Mfn2 during apoptosis. *The Journal of cell biology* **159**, 931-938

36. Dai, X. Y., Huang, X. R., Zhou, L., Zhang, L., Fu, P., Manthey, C., Nikolic-Paterson, D. J., and Lan, H. Y. (2016) Targeting c-fms kinase attenuates chronic aristolochic acid nephropathy in mice. *Oncotarget* **7**, 10841-10856

37. Sarkar, S., Siddiqui, A. A., Mazumder, S., De, R., Saha, S. J., Banerjee, C., Iqbal, M. S., Adhikari, S., Alam, A., Roy, S., and Bandyopadhyay, U. (2015) Ellagic Acid, a Dietary Polyphenol, Inhibits Tautomerase Activity of Human Macrophage Migration Inhibitory Factor and Its Pro-inflammatory Responses in Human Peripheral Blood Mononuclear Cells. *Journal of agricultural and food chemistry* **63**, 4988-4998

38. Zhu, G., Tang, Y., Geng, N., Zheng, M., Jiang, J., Li, L., Li, K., Lei, Z., Chen, W., Fan, Y., Ma, X., Li, L., Wang, X., and Liang, X. (2014) HIF-alpha/MIF and NF-kappaB/IL-6 axes contribute to the recruitment of CD11b+Gr-1+ myeloid cells in hypoxic microenvironment of HNSCC. *Neoplasia* **16**, 168-179

39. Berkova, Z., Wang, S., Ao, X., Wise, J. F., Braun, F. K., Rezaeian, A. H., Sehgal, L., Goldenberg, D. M., and Samaniego, F. (2014) CD74 interferes with the expression of fas receptor on the surface of lymphoma cells. *Journal of experimental & clinical cancer research : CR* **33**, 80

40. Lantner, F., Starlets, D., Gore, Y., Flaishon, L., Yamit-Hezi, A., Dikstein, R., Leng, L., Bucala, R., Machluf, Y., Oren, M., and Shachar, I. (2007) CD74 induces TAp63 expression leading to B-cell survival. *Blood* **110**, 4303-4311

41. Catz, S. D., and Johnson, J. L. (2001) Transcriptional regulation of bcl-2 by nuclear factor kappa B and its significance in prostate cancer. *Oncogene* **20**, 7342-7351

42. Andas, A. R., Abdul, A. B., Rahman, H. S., Sukari, M. A., Abdelwahab, S. I., Samad, N. A., Anasamy, T., and Arbab, I. A. (2015) Dentatin from Clausena excavata Induces Apoptosis in HepG2 Cells via Mitochondrial Mediated Signaling. *Asian Pacific journal of cancer prevention : APJCP* **16**, 4311-4316

43. Pagliari, L. J., Perlman, H., Liu, H., and Pope, R. M. (2000) Macrophages require constitutive NF-kappaB activation to maintain A1 expression and mitochondrial homeostasis. *Molecular and cellular biology* **20**, 8855-8865

44. Patten, D. A., Wong, J., Khacho, M., Soubannier, V., Mailloux, R. J., Pilon-Larose, K., MacLaurin, J. G., Park, D. S., McBride, H. M., Trinkle-Mulcahy, L., Harper, M. E., Germain, M., and Slack, R. S. (2014) OPA1-dependent cristae modulation is essential for cellular adaptation to metabolic demand. *The EMBO journal* **33**, 2676-2691

45. Alavi, M. V., and Fuhrmann, N. (2013) Dominant optic atrophy, OPA1, and mitochondrial quality control: understanding mitochondrial network dynamics. *Molecular neurodegeneration* **8**, 32

46. Subbannayya, T., Variar, P., Advani, J., Nair, B., Shankar, S., Gowda, H., Saussez, S., Chatterjee, A., and Prasad, T. S. (2016) An integrated signal transduction network of macrophage migration inhibitory factor. *Journal of cell communication and signaling* **10**, 165-170

47. Hoesel, B., and Schmid, J. A. (2013) The complexity of NF-kappaB signaling in inflammation and cancer. *Mol Cancer* **12**, 86

48. Oeckinghaus, A., and Ghosh, S. (2009) The NF-kappaB family of transcription factors and its regulation. *Cold Spring Harb Perspect Biol* **1**, a000034

49. Zheng, C., Yin, Q., and Wu, H. (2011) Structural studies of NF-kappaB signaling. *Cell Res* **21**, 183-195

50. Li, N., Yi, Z., Wang, Y., Zhang, Q., Zhong, T., Qiu, Y., Wu, Z., and Tang, X. (2012) Differential proteomic analysis of HL60 cells treated with secalonic acid F reveals caspase 3-induced cleavage of Rho GDP dissociation inhibitor 2. *Oncology reports* **28**, 2016-2022

51. Waterborg, J. H., and Matthews, H. R. (1984) The lowry method for protein quantitation. *Methods Mol Biol* **1**, 1-3

52. Cheng, S. P., Liu, C. L., Chen, M. J., Chien, M. N., Leung, C. H., Lin, C. H., Hsu, Y. C., and Lee, J. J. (2015) CD74 expression and its therapeutic potential in thyroid carcinoma. *Endocr Relat Cancer* **22**, 179-190

Figure legends

Figure 1: Loss of mitochondrial integrity and increased fission upon MIF downregulation in AGS cells. (A) Immunoblot analysis of MIF in AGS cells treated with siMIF; the cells were harvested at the indicated time points and the cell lysates were immunoblotted to check the transfection efficiency. Actin was used as the loading control. Densitometric values of the immunoblot are presented below each band. (B) Phase-contrast microscopic images (taken in Leica DMI 3000B inverted microscope with 10X objective lens) of un-transfected control, control siRNA and siMIF-treated AGS cells; Scale bar, 10 μm. (C) Measurement of AGS cell proliferation by [³H] thymidine incorporation in un-transfected control, control siRNA and siMIF-treated AGS cells (D) MTT reduction assay for cellular dehydrogenase activity in siMIF-treated AGS cells compared to control siRNA treated set. (E) Flow cytometric analysis to follow mitochondrial transmembrane potential (ΔΨm) after MIF knockdown in AGS cells; red signal in the cytofluorogram indicated JC-1 aggregates fluorescing at 590 nm and green indicated JC-1 monomers (corresponding to depolarized mitochondria) fluorescing at 530 nm; Percentage values represent number of cells emitting red or green signals corresponding to the cells with polarized and depolarized mitochondria. 10,000 events were screened per experimental set and a representative flow cytometry scatter plot of gated cell population is presented. Percentages of cells are presented in each quadrant with respective colour. (F) ATP content in control siRNA and siMIF-treated AGS cells were evaluated with the help of luciferase reaction-based technique and Relative Light Unit (RLU) values are presented. (G) High-resolution confocal micrographs demonstrate mitochondrial fragmentation in cells transfected with control siRNA and siMIF at different time points 24 h, 48 h, and 72 h post transfection in AGS cells; scale bar represents 10 μm; 80-100 cells were randomly screened and a single field was randomly selected for demonstration. Enlarged images of the region of interest (ROI) were prepared by digital zooming of the selected region for clear visualization of mitochondrial filaments. Quantification of the mitochondrial length distribution of control and siMIF-treated cells by LAS-X software are presented below each set of micrographs; 80-100 cells were screened for the analysis. Scatter plots adjacent to each micrograph represent mitochondrial length distribution. Each color represents a specific filament length. (H) Ratio of mitochondrial DNA (mtDNA) to nuclear DNA (nDNA) in control siRNA and siMIF-treated cells. All experiments were done in triplicate. A detail of each method is described under "Experimental procedures". **P < 0.01, ***P < 0.001 versus control calculated by unpaired student's t-test and ns = non-significant, *P < 0.05, **P < 0.01, ***P < 0.001 versus control calculated by ANOVA followed by Bonferroni's post hoc test.

Figure 2: MIF silencing induces apoptosis in AGS cells. (A) Flow cytometric analysis of control siRNA and siMIF-treated AGS cells at different time points of 24 h, 48 h, and 72 h to determine cell death by FITC-annexin V/PI staining. 10,000 events were screened per experimental set and a representative flow cytometry scatter plot of gated cell population was presented. Quadrant Q2 and

Q4 correspond to late and early apoptosis respectively and cumulatively represent annexin V binding to cells undergoing apoptosis. Percentages of cells are presented in each respective quadrant. Data presented are one of the representatives of three independent experiments. (B) Cell cycle analysis of control siRNA and siMIF-treated AGS cells. (C) Confocal micrographs depicting Bax translocation to mitochondria in control siRNA and siMIF-treated AGS cells; 4th panel represents the enlarged view of the selected ROI along with the corresponding Pearson's correlation coefficient to quantify the distribution of Bax on mitochondria. Scale bar represents 10 μm. 5th column represents the line scan plot of the cyan line indicating localization of Bax (green) on mitochondria (red). A detail of each method is described under "Experimental procedures".

Figure 3. Loss of mitochondrial membrane potential and increased fission upon MIF downregulation interfere with HepG2 cell viability. (A) Immunoblot analysis of MIF in control siRNA and siMIF-treated HepG2 cells. Densitometric values of the bands in immunoblots are provided below blot images. Actin was used as the loading control. (B) Cell viability test by MTT reduction assay in control siRNA and siMIF-treated HepG2 cells. (C) Flow cytometric analysis to follow mitochondrial transmembrane potential (ΔΨm) upon MIF knock down. Percentage values represent proportion of cells emitting the respective signals. (D) High-resolution confocal micrographs to demonstrate mitochondrial fragmentation in control siRNA and siMIF-treated HepG2 cells; Scale bar represents 10 μm; 80-100 cells were randomly screened and a single cell was randomly selected for demonstration of mitochondrial fission at the single-cell level; enlarged images of the region of interest (ROI) were prepared by digital zooming of the selected region for clear visualization of mitochondrial filaments. Quantification of the mitochondrial length distribution of control and MIF-silenced cell by LAS-X software is provided beneath each set; 80-100 cells were screened for the analysis. Scatter plots adjacent to each micrograph represented mitochondrial length distribution. Each color represents a specific filament length indicated in the inset of the scatter plot. (E) Flow cytometric analysis following FITC-annexin V/PI staining of control siRNA and siMIF-treated HepG2 cells to determine apoptosis. Quadrant Q2 and Q4 correspond to late and early apoptosis respectively and cumulatively represent annexin V binding to cells undergoing apoptosis. All experiments were done in triplicate. A detail of each method is described under "Experimental procedures". ns = non-significant, *P < 0.05, **P < 0.01 versus control calculated by unpaired student's t-test.

Figure 4. Reduced viability due to MIF-knockdown is positively associated with elevated mitochondrial fission in HeLa and HCT 116 cells. (A) Cell viability test by MTT reduction assay in control siRNA and siMIF treated HeLa cells. (B) High-resolution confocal micrographs to demonstrate mitochondrial fragmentation in control siRNA and siMIF treated HeLa cells; Scale bar represents 10 μm. (C) Cell viability test by MTT reduction assay in control siRNA and siMIF treated HCT 116 cells. (D) High-resolution confocal micrographs to demonstrate mitochondrial

19

fragmentation in HCT control siRNA and siMIF treated HCT 116 cells; Scale bar represents 10 μm. 80-100 cells were randomly screened and subjected to analysis; a single cell was randomly selected for demonstrating mitochondrial fission at the single-cell level; enlarged images of the region of interest (ROI) were prepared by digital zooming of the selected region for clear visualization of mitochondrial filaments. Quantification of the mitochondrial length distribution of control and MIF-silenced cell by LAS-X software is provided beneath each set. Scatter graph adjacent to each micrograph represent mitochondrial length distribution. Each color represents a specific filament length indicated in the inset of the scatter plot. A detail of each method is described under "Experimental procedures". ns = non-significant, *P < 0.05, **P < 0.01 versus control calculated by unpaired student's t-test.

Figure 5: MIF depletion increases pro-apoptotic protein expression and subsequent caspase activation in AGS cells. (A) Immunoblot analysis of apoptotic mediators in control siRNA and siMIF treated AGS cells. Numerical values corresponding to the densitometric analysis of the immunoblot data are provided below the bands. (B) ELISA to detect cytochrome C release in the cytosol in control siRNA and siMIF treated AGS cells. (C) Caspase 3 activity to analyze apoptosis in control siRNA and siMIF treated AGS cells. All experiments were done in triplicate. (D) Flow cytometric analysis of AGS cells to determine apoptosis in control siRNA, siMIF treated and siMIF + Ac-DEVD-CHO treated AGS cells. 10,000 events were screened per experimental set and a representative flow cytometry scatter plot of gated cell population is presented. Quadrants Q2 and Q4 correspond to late and early apoptosis respectively and cumulatively represent annexin V binding to cells undergoing apoptosis. Percentages of cells are presented in each respective quadrant. Data presented are one of the representatives of three independent experiments. A detail of each method is described under "Experimental procedures". **P < 0.01 and ***P < 0.001 versus control calculated by unpaired student's t-test.

Figure 6: MIF supplementation rescues MIF-knockdown-induced increased mitochondrial fission and loss of cell viability. (A) Cell viability test by MTT reduction assay in control siRNA, siMIF and siMIF + MIF treated cells. (B) High-resolution confocal micrographs to demonstrate mitochondrial fragmentation in AGS cells of siMIF (left panel) and siMIF + MIF treated cells (right panel) respectively; scale bar, 10 μm; 80-100 cells were randomly screened and a single cell was randomly selected and digitally zoomed for demonstration of mitochondrial fission; enlarged images are presented as ROI enlarged. Quantification of the mitochondrial length distribution by LAS-X software has been provided along with each set; 80-100 cells were screened for the analysis. Scatter graph adjacent to each micrograph represented mitochondrial length distribution. Each color represents a specific filament length. All experiments were done in triplicate. A detail of each method is described under "Experimental procedures". ns = non-significant, ***P < 0.001 versus control; ##P

20

< 0.01 versus siMIF treatment calculated by ANOVA followed by Bonferroni's post hoc test. ns = non-significant, [#]P < 0.05, [##]P < 0.01 versus siMIF treatment calculated by unpaired student's t-test.

Figure 7: Effect of MIF knockdown on the expression of key proteins modulating mitochondrial fission in AGS cells. (A) Western blot analysis to follow the expression of fission-regulator Drp1, phosphorylated Drp1 i.e. p-Drp1-s637 and p-Drp1-s637 in the control siRNA, siMIF-treated cells. Actin was used as the loading control; numerical values corresponding to the densitometric analysis of the immunoblot data are provided below the bands.   (B) Confocal micrographs to demonstrate Drp1 translocation to mitochondria in the control siRNA, siMIF-treated cells. 2nd and 4th rows represent the zoomed view of corresponding fields presented in 1st and 3rd rows respectively. 3rd column represented the merged image whereas 4th column represent the enlarged view of the selected regions of interest (ROI) along with the Pearson's correlation coefficient, quantifying the distribution of Drp1 on mitochondria. Scale bar, 10 μm. 5th column represents the line scan plot of the cyan line presented in merge panel. (C) Immunoblot analysis of Drp1 to check the transfection efficiency in control siRNA and siDrp1-treated cells harvested at the indicated time points. Actin was used as the loading control. Densitometric analysis of the immunoblot data is presented below the bands. (D) High-resolution confocal micrographs to demonstrate mitochondrial fragmentation in control siRNA, siMIF and siMIF + siDrp1 double transfected AGS cells; scale bar represents 10 μm. 80-100 cells were randomly screened and a single cell was randomly selected for demonstration of mitochondrial fission at the single-cell level; enlarged images of the region of interest (ROI) were prepared by digital zooming of the selected region for clear visualization of mitochondrial filaments. Quantification of the mitochondrial length distribution by LAS-X software has been provided along with each set; 80-100 cells were screened for the analysis. Scatter plots adjacent to each micrograph represented mitochondrial length distribution. Each color represents a specific filament length. A detail of each method is described under "Experimental procedures". ns = non-significant, *P < 0.05, versus control and ns = non-significant, [#]P < 0.05, [##]P <0.01 versus siMIF treatment calculated by ANOVA followed by Bonferroni's post hoc test.

Figure 8: Silencing of Drp1 offers partial protection against MIF depletion in AGS cells. (A) Cell viability test by MTT reduction assay in control siRNA, siMIF and siMIF + siDrp1 double transfected AGS cells. (B) Flow cytometric analysis to determine the apoptosis in control siRNA, siMIF and siMIF + siDrp1 double transfected cells with the help of FITC-annexin V/PI staining. 10,000 events were screened per experimental set and a representative flow cytometry scatter plot of gated cell population is presented. Quadrants Q2 and Q4 correspond to late and early apoptosis respectively and cumulatively represent annexin V binding to cells undergoing apoptosis. Percentages of cells are presented in each respective quadrant. Data presented are one of the representatives of the three independent experiments. (C) Flow cytometric analysis to follow mitochondrial transmembrane potential (ΔΨm) in control siRNA, siMIF and siMIF + siDrp1 double transfected cells; red signal in

the scatter plot correspond to JC-1 aggregates fluorescing at 590 nm and green indicated JC-1 monomers (corresponding to depolarized mitochondria) fluorescing at 530 nm; Percentage values represent number of cells emitting red or green signals corresponding to the cells with polarized or depolarized mitochondria respectively. 10,000 events were screened per experimental set and a representative flow cytometry scatter plot of gated cell population is presented. (D) ATP content in control siRNA, siMIF and siMIF + siDrp1 double transfected cells measured by luciferase reaction-based technique and Relative Light Unit (RLU) values were presented as fold relative to control siRNA-treated cells. (E) Immunoblot analysis to follow the expression of Bcl-2, Bcl-xL, Bax, MIF and Drp1 in the control siRNA, siMIF, siDrp1 and siMIF + siDrp1 double transfected cells. Actin was used as the loading control; numerical values corresponding to the densitometric analysis of the immunoblot data are provided below the bands. (F) Immunoblot analysis of key mitochondrial fusion mediators Opa1, Mfn1, Mfn2 in the in the control siRNA, siMIF-treated AGS cells; Actin was used as the loading control; numerical values corresponding to the densitometric analysis of the immunoblot data are provided below the bands. A detail of each method is described under "Experimental procedures". ***$P < 0.001$ versus control; [#]$P < 0.05$ versus siMIF treatment calculated by ANOVA followed by Bonferroni's post hoc test; values ns = non-significant versus control calculated by student's t test.

Figure 9: MIF regulates the activation of NF-κB in AGS cells which is instrumental in maintaining mitochondrial dynamic balance. (A) Confocal super resolution immunofluorescent micrographs to demonstrate nuclear translocation of NF-κB in control siRNA, siMIF and siMIF + MIF treated AGS cells. NF-κB (green) was immunostained by anti-NF-κB (p65) primary and alexa fluor 488 conjugated goat anti-rabbit secondary antibodies; Nuclei (blue) were stained with DAPI; 3rd panel represent the merged images of NF-κB and nucleus; Pearson's correlation coefficient for quantifying the distribution of NF-κB within the nucleus is presented adjacent to each set. Scale bar, 10 μm. The image presented is a representative of one of the three independent experiments and about 100 cells per experimental set were screened for the analysis. (B) Western blot analysis of NF-κB in control siRNA and siNF-κB treated AGS cells harvested at the indicated time points to check the transfection efficiency. Actin was used as the loading control; numerical values corresponding to the densitometric analysis of the immunoblot data are provided below the bands. (C) Cell viability test by MTT reduction assay in control siRNA and siNF-κB treated AGS cells. (D) Flow cytometric analysis of control siRNA and siNF-κB treated AGS cells to determine the cell death by FITC-annexin V/PI staining. 10,000 events were screened per experimental set and a representative flow cytometry scatter plot of gated cell population is presented. Quadrants Q2 and Q4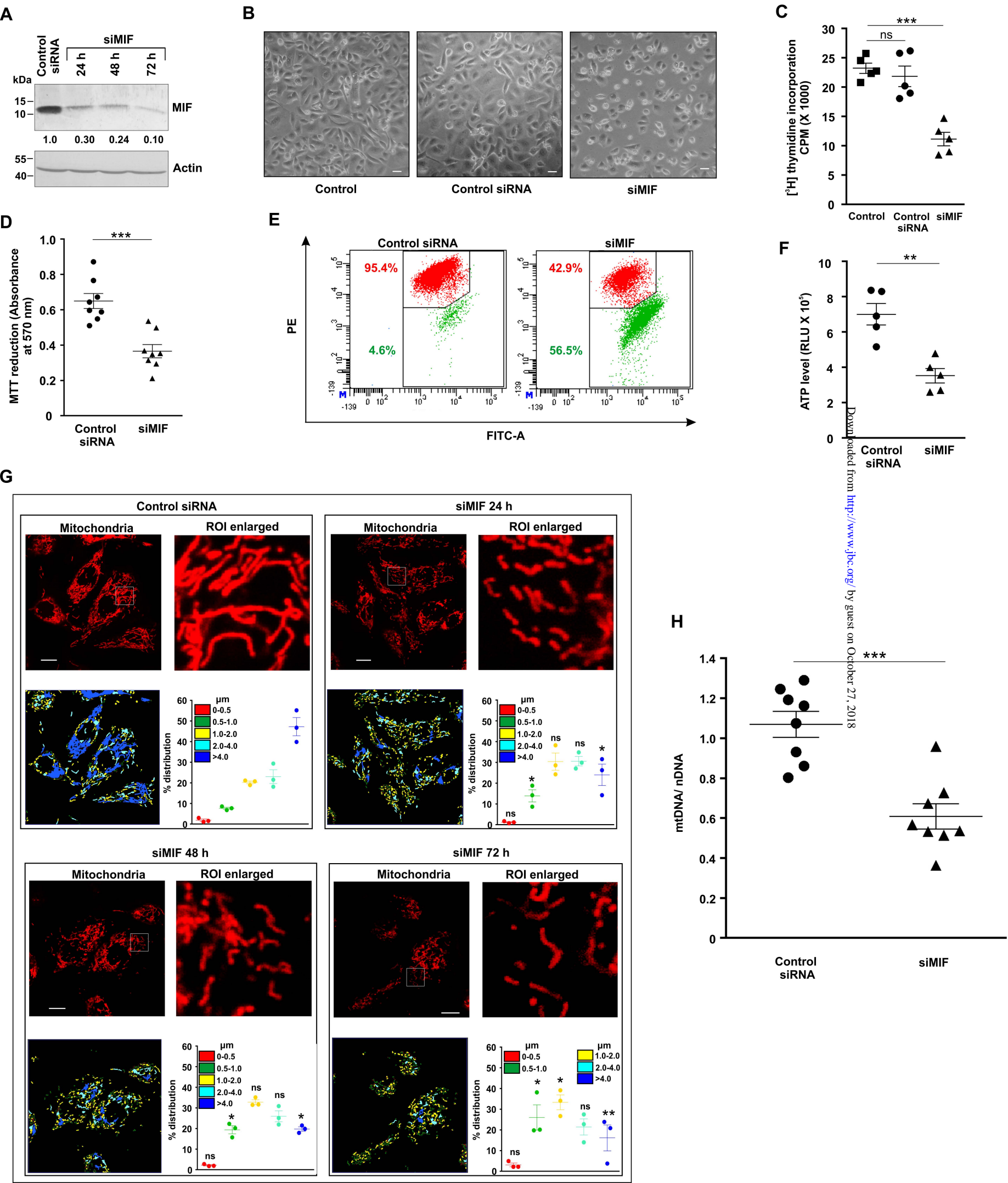 correspond to late and early apoptosis respectively and cumulatively represent annexin V binding to cells undergoing apoptosis. Percentages of cells are presented in each respective quadrant. Data presented are one of the representatives of three independent experiments. (E) Live cell confocal micrographs to demonstrate mitochondrial

fragmentation in control siRNA and siNF-κB treated AGS cells; scale bar, 10 μm; 80-100 cells were randomly screened and a single cell was randomly selected for demonstration of mitochondrial fission at the single-cell level; enlarged images of the region of interest (ROI) were prepared by digital zooming of the selected region for clear visualization of mitochondrial filaments. Quantification of the mitochondrial length distribution of control and NF-κB-silenced cells by LAS-X software are provided along with each set. Scatter plot graph adjacent to each micrograph represent mitochondrial length distribution. Each color represents a specific filament length. (F) Flow cytometric analysis of control siRNA, siMIF, siMIF + MIF and siMIF + MIF + siNF-κB treated AGS cells to determine the contributing action of NF-κB knock down in MIF-depleted AGS cells supplemented with recombinant MIF on cell death by apoptosis. 10,000 events were screened per experimental set and a representative flow cytometry scatter plot of gated cell population was presented. Quadrants Q2 and Q4 correspond to late and early apoptosis respectively and cumulatively represent annexin V binding to cells undergoing apoptosis. Percent cells are presented in each respective quadrant. Data presented are one of the representatives of three independent experiments. All experiments were done in triplicate. A detail of each method is described under "Experimental procedures". ns = non-significant, *P < 0.05, **P < 0.01 versus control calculated by unpaired student's t-test.

Figure 10: NF-κB over expression significantly ameliorates cell death and mitochondrial pathology induced by MIF depletion in AGS cells. (A) Flow cytometric analysis to follow mitochondrial transmembrane potential (ΔΨm) in 'Empty vector', 'siMIF' and 'siMIF + pNF-κB p65' treatment in AGS cells; pNF-κB p65 is the NF-κB over expression plasmid; red signal in the scatter plot indicated JC-1 aggregates fluorescing at 590 nm and green indicated JC-1 monomers (corresponding to depolarized mitochondria) fluorescing at 530 nm; Percentage values represent number of cells emitting red or green signals corresponding to the cells with polarized and depolarized mitochondria. 10,000 events were screened per experimental set and a representative flow cytometry scatter plot of gated cell population was presented. (B) High-resolution confocal micrographs to demonstrate mitochondrial fragmentation in 'Empty vector', 'siMIF' and 'siMIF + pNF-κB p65' treated AGS cells; scale bar, 10 μm; 80-100 cells were randomly screened and a single field was randomly selected for demonstration. Enlarged images of the region of interest (ROI) were prepared by digital zooming of the selected region for clear visualization of mitochondrial filaments. Quantification of the mitochondrial length distribution of control and MIF-silenced cell by LAS-X software are presented below each set of micrographs; 80-100 cells were screened for the analysis. Scatter plots adjacent to each micrograph represent mitochondrial length distribution. Each color represents a specific filament length. (C) Flow cytometric analysis of apoptosis in AGS cells treated with 'Empty vector', 'siMIF' and 'siMIF + pNF-κB p65'with the help of FITC-annexin V/PI staining. 10,000 events were screened per experimental set and a representative flow cytometry scatter plot of gated cell population is presented. Quadrants Q2 and Q4 correspond to late and early apoptosis

respectively and cumulatively represent annexin V binding to cells undergoing apoptosis. Percentages of cells are presented in each respective quadrant. Data presented are one of the representatives of three independent experiments. All experiments were done in triplicate. A detail of each method is described under "Experimental procedures". ns = non-significant, *P < 0.05, **P < 0.01 versus control and ns = non-significant, #P < 0.05, ##P < 0.01 versus siMIF treatment calculated by ANOVA followed by Bonferroni's post hoc test.

Figure 11: CD74-MIF signaling is necessary for AGS cell survival and maintenance of mitochondrial structural integrity. (A) Cellular expression and localization of MIF on cell surface in AGS cells by confocal immunofluorescence microscopy; MIF (red) was immunostained by anti-MIF primary and alexa fluor 647 conjugated goat anti-rabbit secondary antibodies; 3rd panel represented the merged image of differential interference contrast (DIC) image of cells with red channel to demonstrate the intracellular localization. Scale bar, 10 μm. (B) MIF tautomerase activity to demonstrate intracellular production as well as secretion of MIF in AGS cells. (C) Immunoblot analysis of MIF in media obtained from AGS cell culture and unused fresh media. (D) [³H] thymidine incorporation assay in control, anti-CD74 antibody-treated and anti-CD74 antibody + MIF treated AGS cells. (E) Immunoblot analysis of CD74 in control siRNA and siCD74 treated AGS cells harvested at the indicated time points to check the transfection efficiency. Actin was used as the loading control; numerical values corresponding to the densitometric analysis of the immunoblot data are provided below the bands. (F) High-resolution confocal micrographs to demonstrate mitochondrial fragmentation in control siRNA and siCD74 treated AGS cells; scale bar, 10 μm; enlarged images of the region of interest (ROI) were prepared by digital zooming of the selected region for clear visualization of mitochondria. Quantification of the mitochondrial length distribution of control and CD74-silenced cell by LAS-X software were documented for each set; 80-100 cells were screened for the analysis. Scatter plot adjacent to each micrograph represented mitochondrial length distribution. Each color represents a specific filament length. (G) Cell viability test by MTT reduction assay in control siRNA and siCD74 treated AGS cells. (H) Immunoblot analysis followed by densitometric assessment of NF-κB and Bax in control siRNA and siCD74 treated AGS cells. Actin was used as endogenous control; numerical values corresponding to the densitometric analysis of the immunoblot data are provided below the bands. (I) Gene expression analysis of NF-κB by real-time PCR in control siRNA and siCD74 treated AGS cells by $2^{-\Delta\Delta Cq}$ method as elaborated in the "Experimental procedures". (J) ATP content was evaluated in control siRNA and siCD74 treated AGS cells with the help of luciferase reaction-based technique and Relative Light Unit (RLU) values were presented. (K) Flow cytometric analysis to follow mitochondrial transmembrane potential (ΔΨm) in control siRNA and siCD74 treated AGS cells; red signal in the scatter plot indicated JC-1 aggregates fluorescing at 590 nm and green indicated JC-1 monomers (corresponding to depolarized mitochondria) fluorescing at 530 nm; Percentage values represent number of cells emitting red or

24

green signals corresponding to the cells with polarized and depolarized mitochondria. 10,000 events were screened per experimental set and a representative flow cytometry scatter plot of gated cell population is presented. (L) Flow cytometric analysis to determine the cell death in control siRNA and siCD74 treated AGS cells with the help of FITC-annexin V/PI staining. 10,000 events were screened per experimental set and a representative flow cytometry scatter plot of gated cell population was presented. Quadrants Q2 and Q4 correspond to late and early apoptosis respectively and cumulatively represent annexin V binding to cells undergoing apoptosis. Percentages of cells are presented in each respective quadrant. Data presented are one of the representatives of three independent experiments. All experiments were done in triplicate. A detail of each method is described under "Experimental procedures". ns = non-significant, *P < 0.05, **P < 0.01 versus control calculated by unpaired student's t-test. ns = non-significant with respect to anti-CD74 treatment, ***P < 0.001 versus control; calculated by ANOVA followed by Bonferroni's post hoc test.

Figure 1

Figure 2
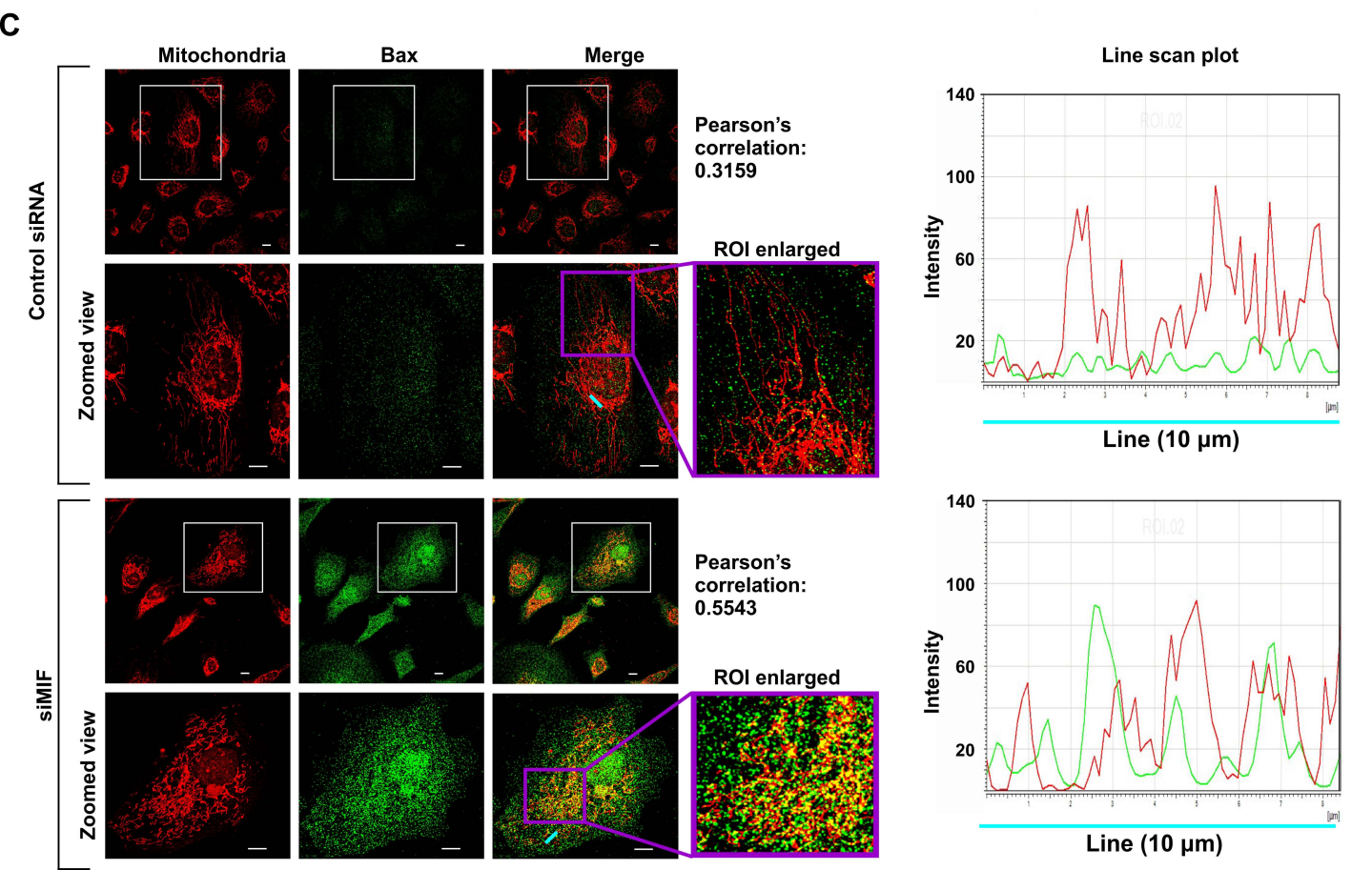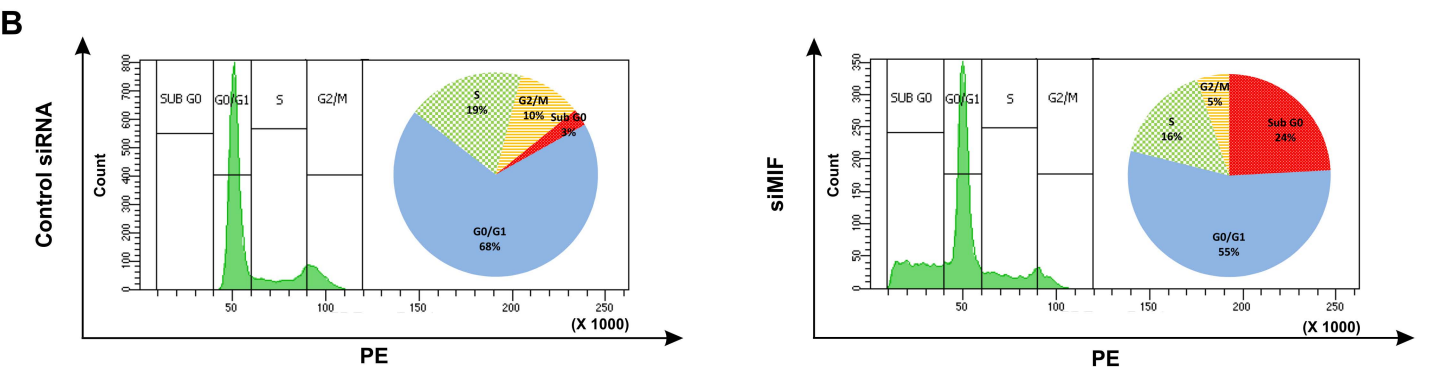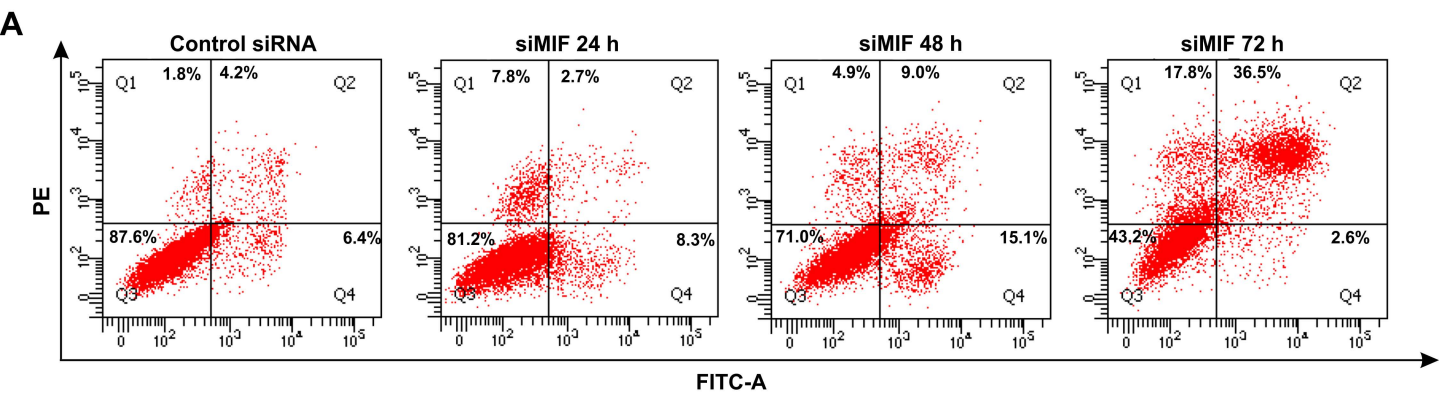
Figure 3
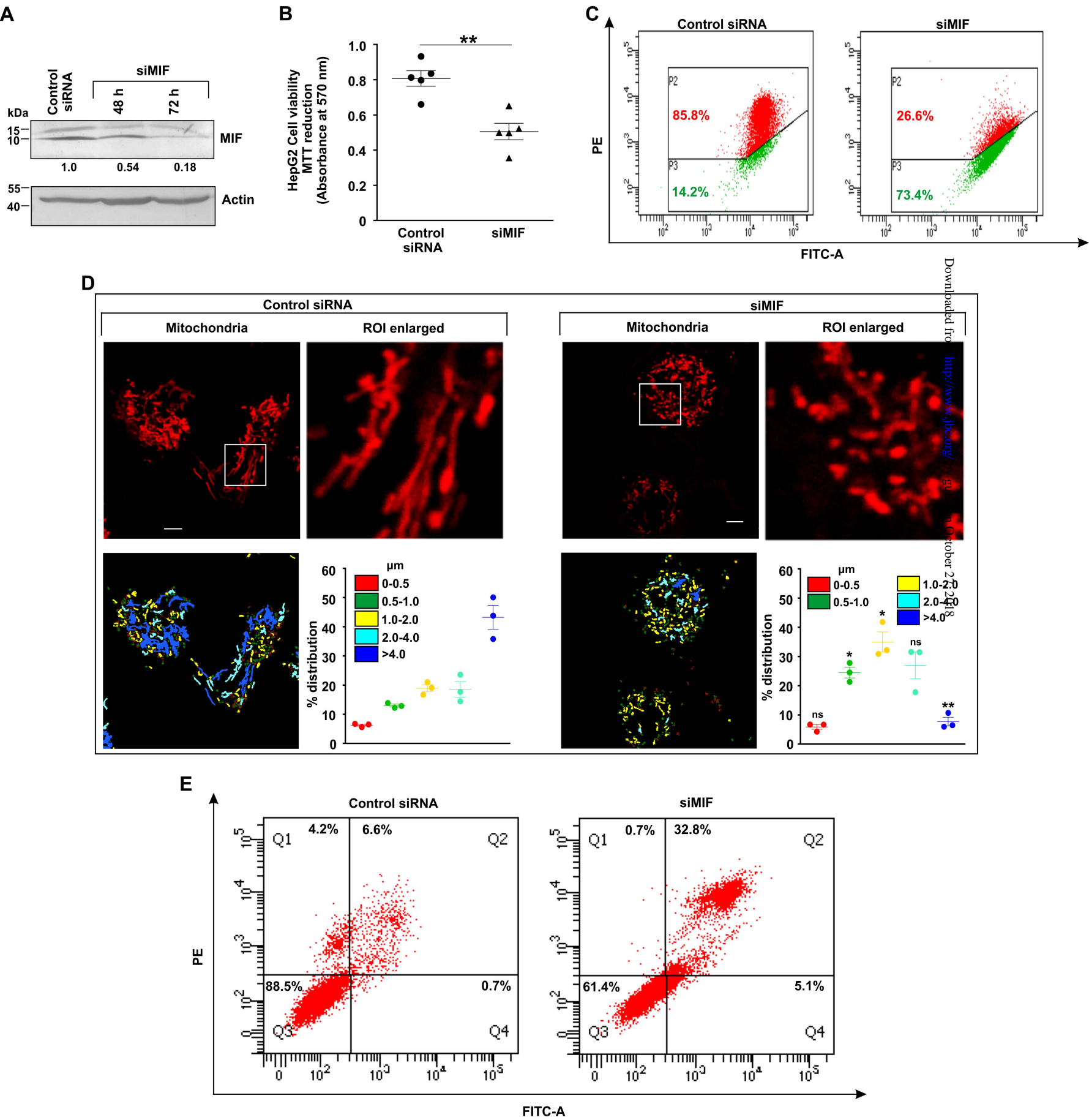
Figure 4
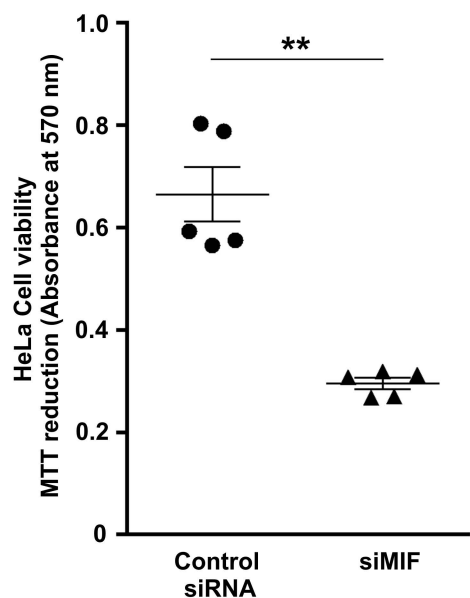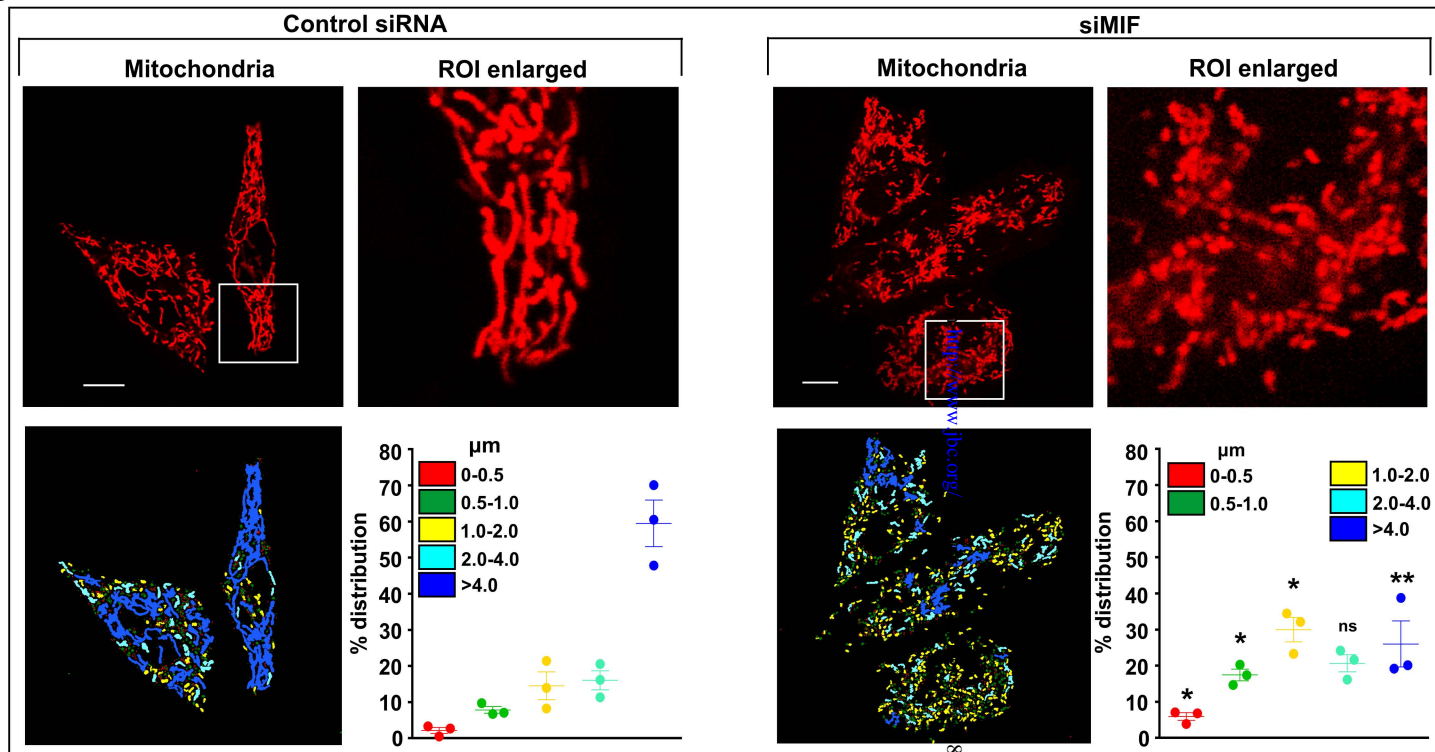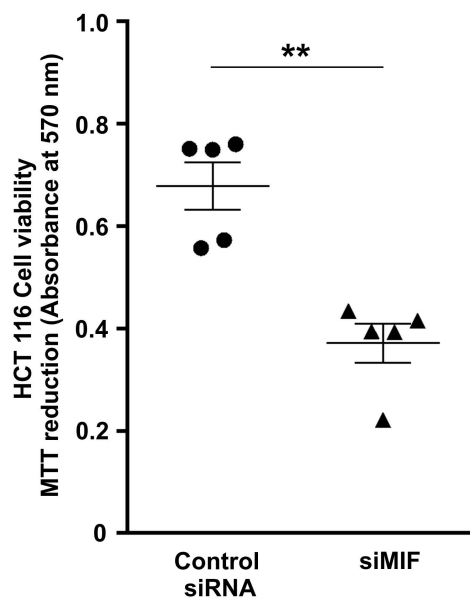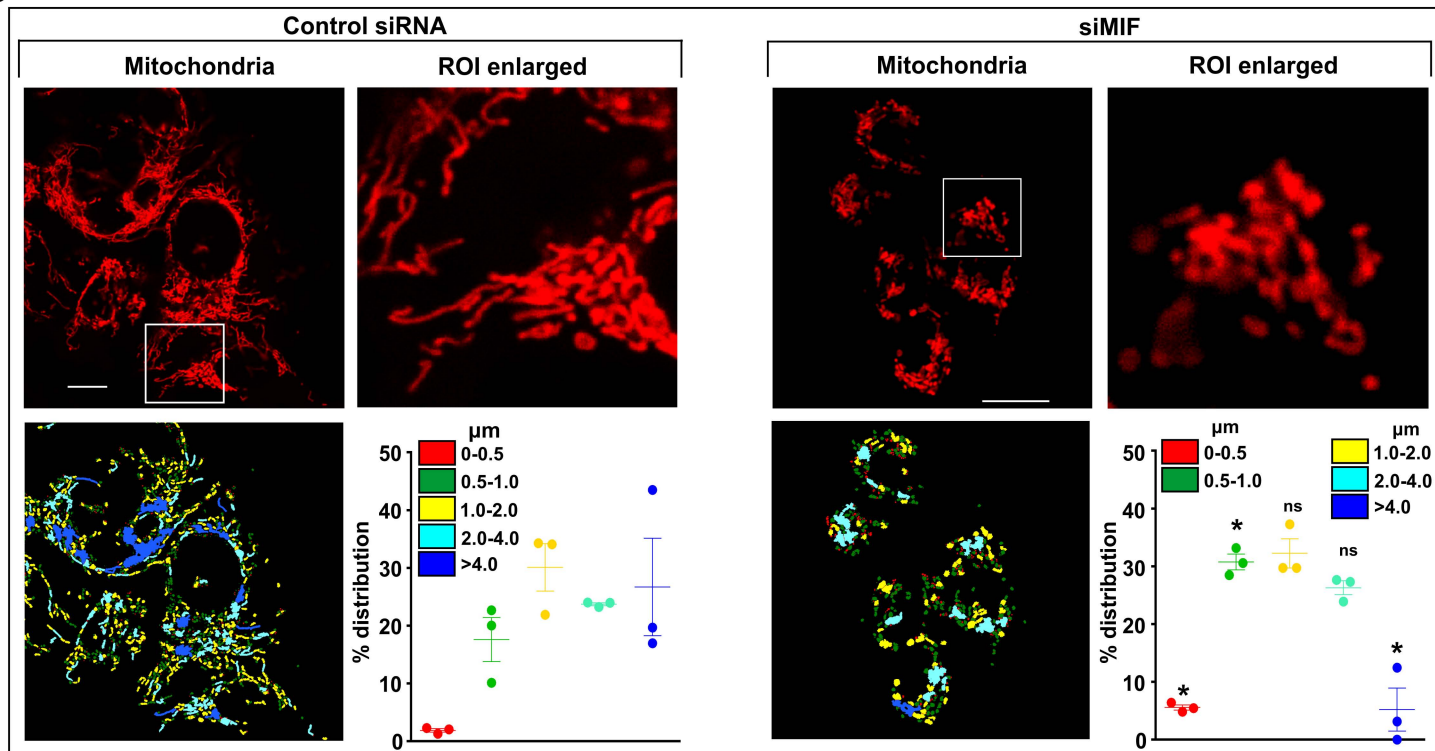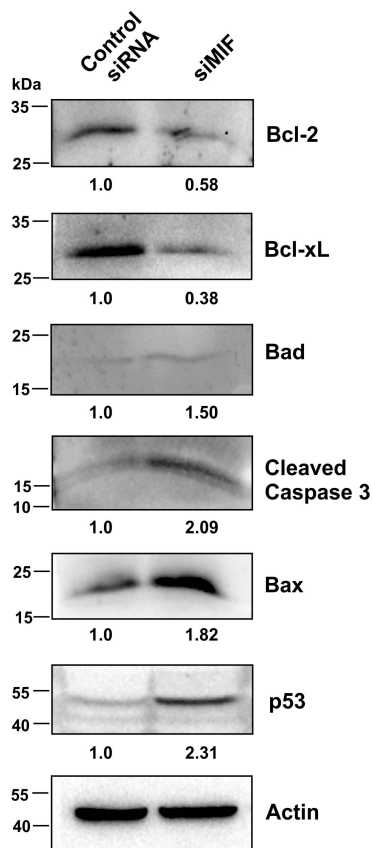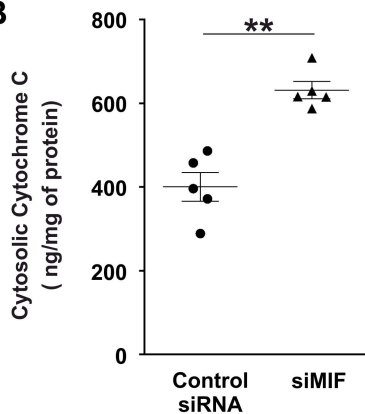
Figure 5

Figure 6

Figure 7

Figure 8

Figure 9

A

	Nucleus	NF-κB	Merge	
Control siRNA				Pearson's correlation: 0.64 ± 0.03
siMIF				Pearson's correlation: 0.37 ± 0.01
siMIF + MIF				Pearson's correlation: 0.66 ± 0.01

B

C

D

E

F
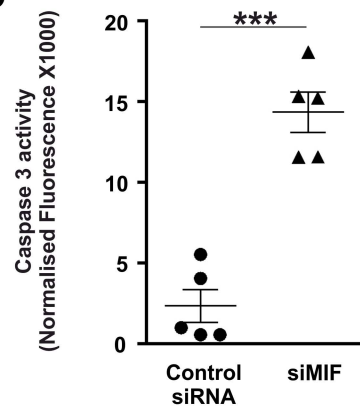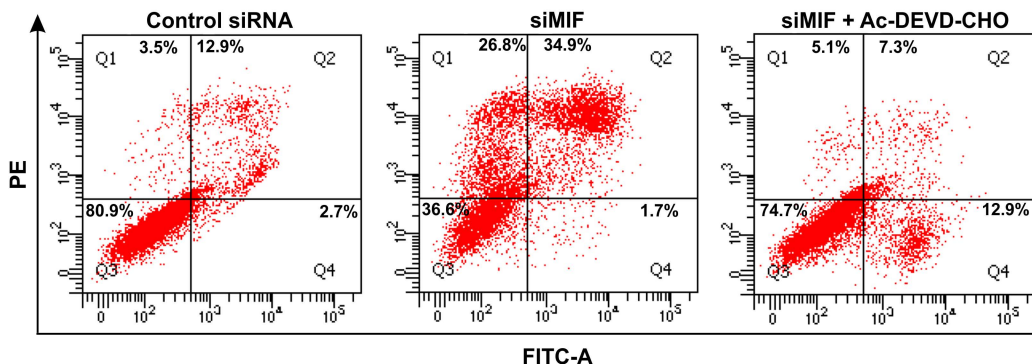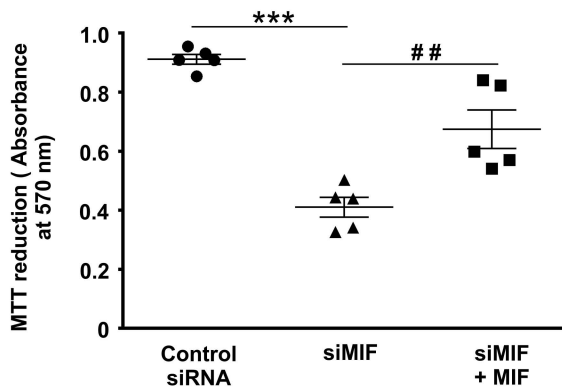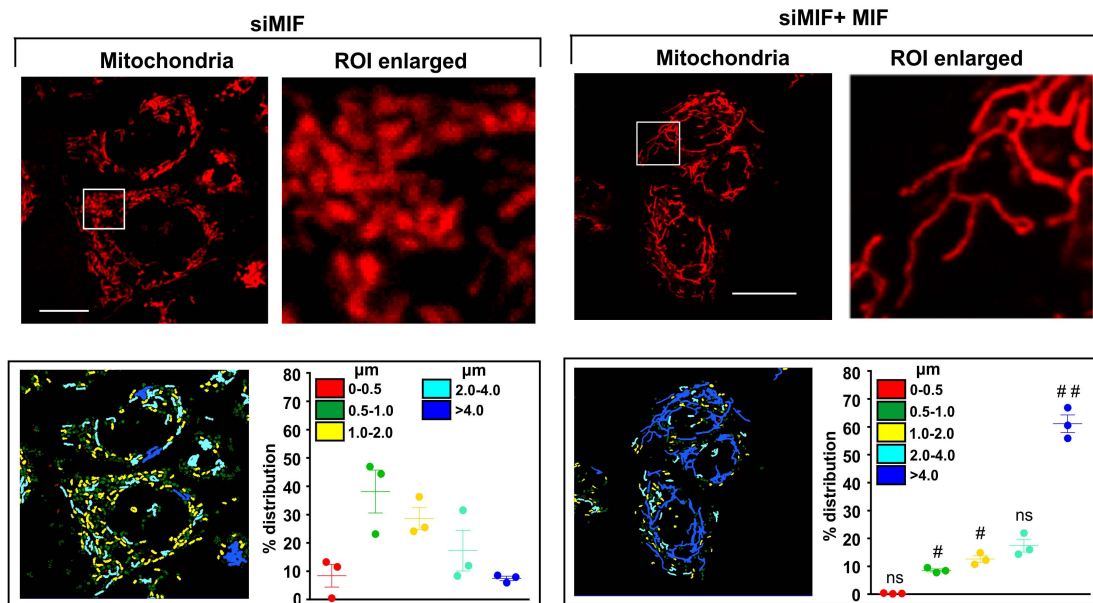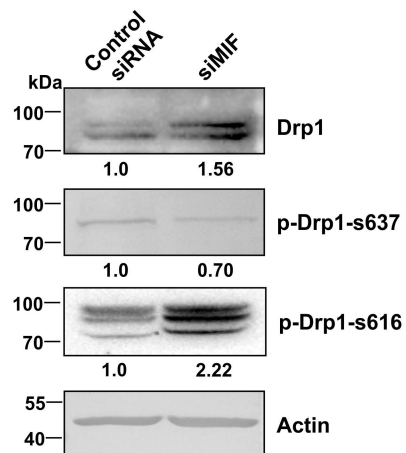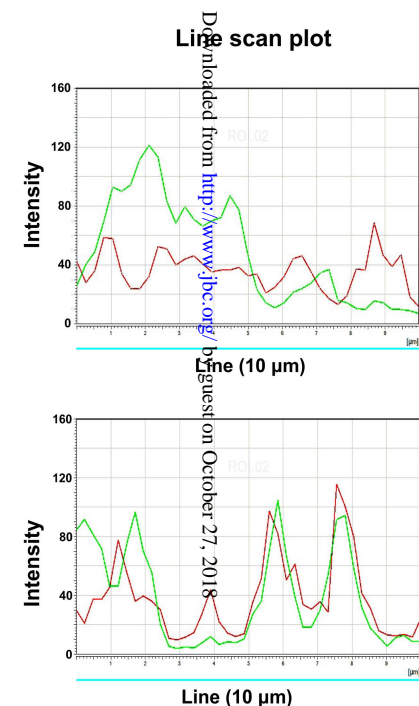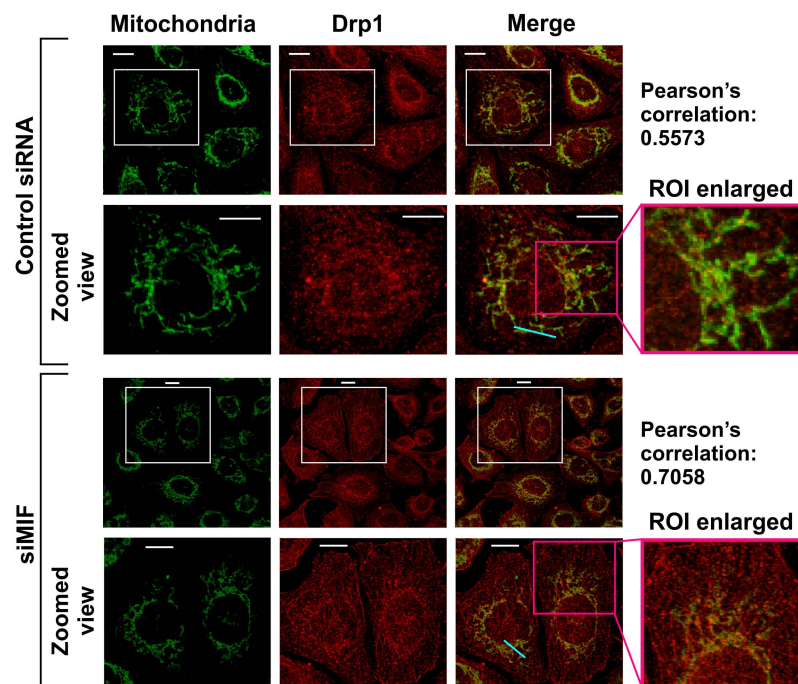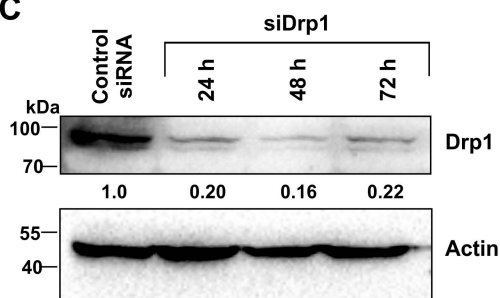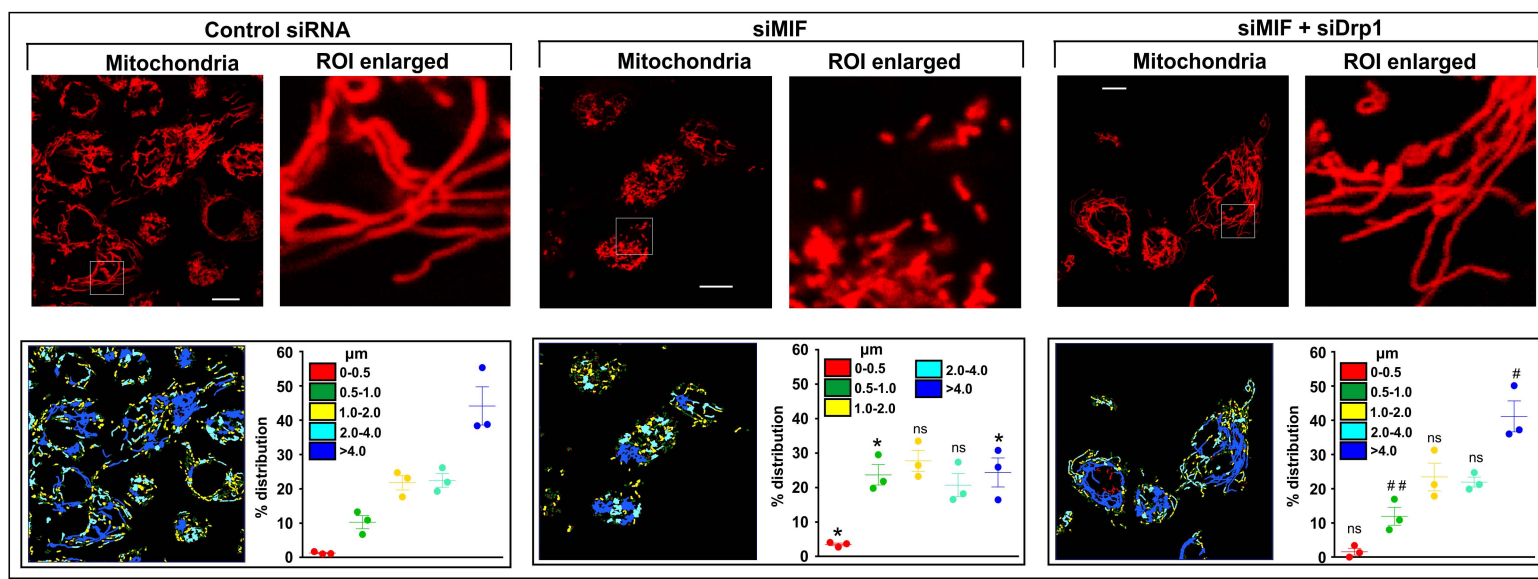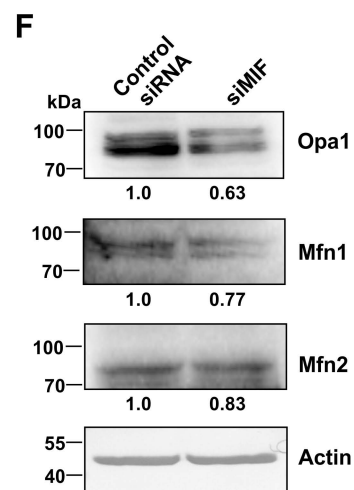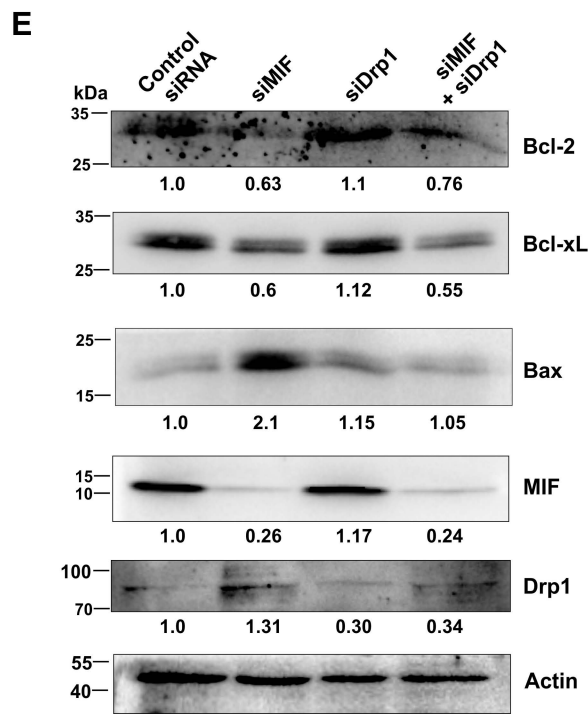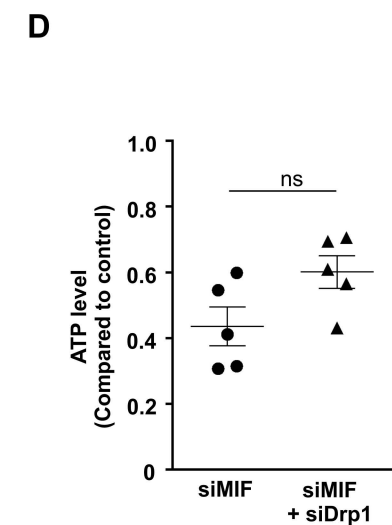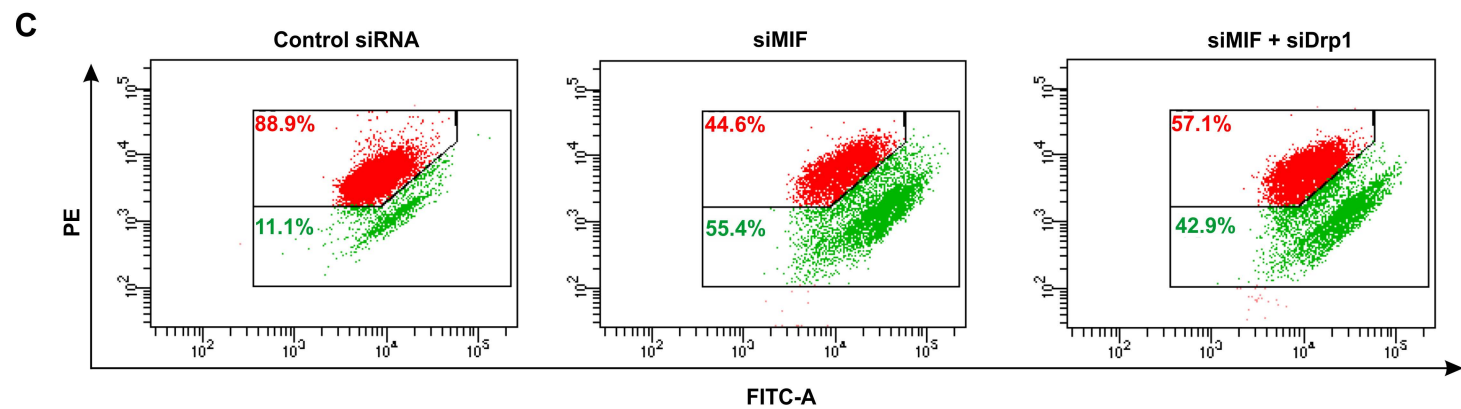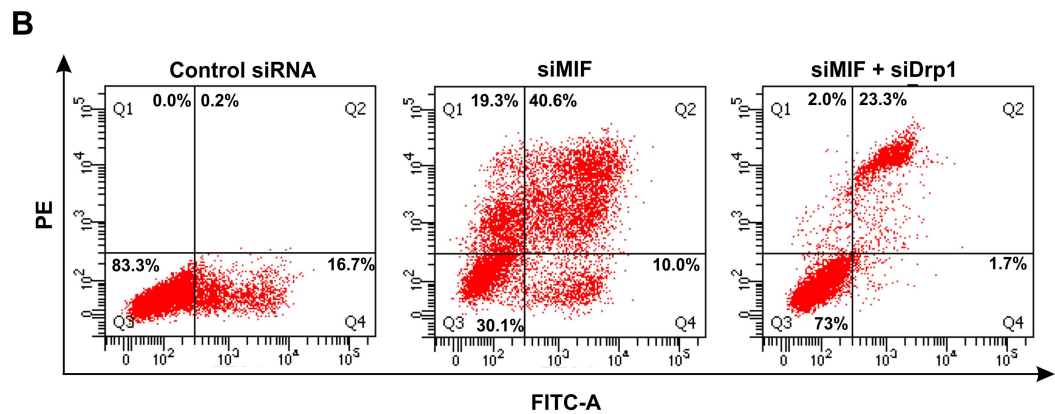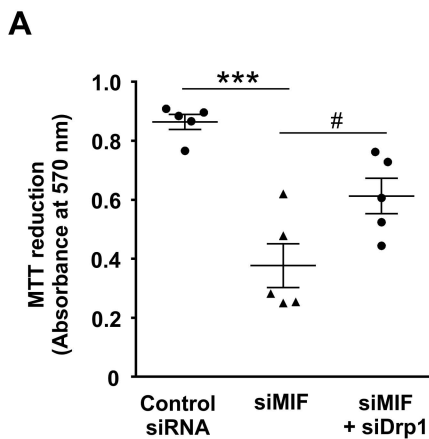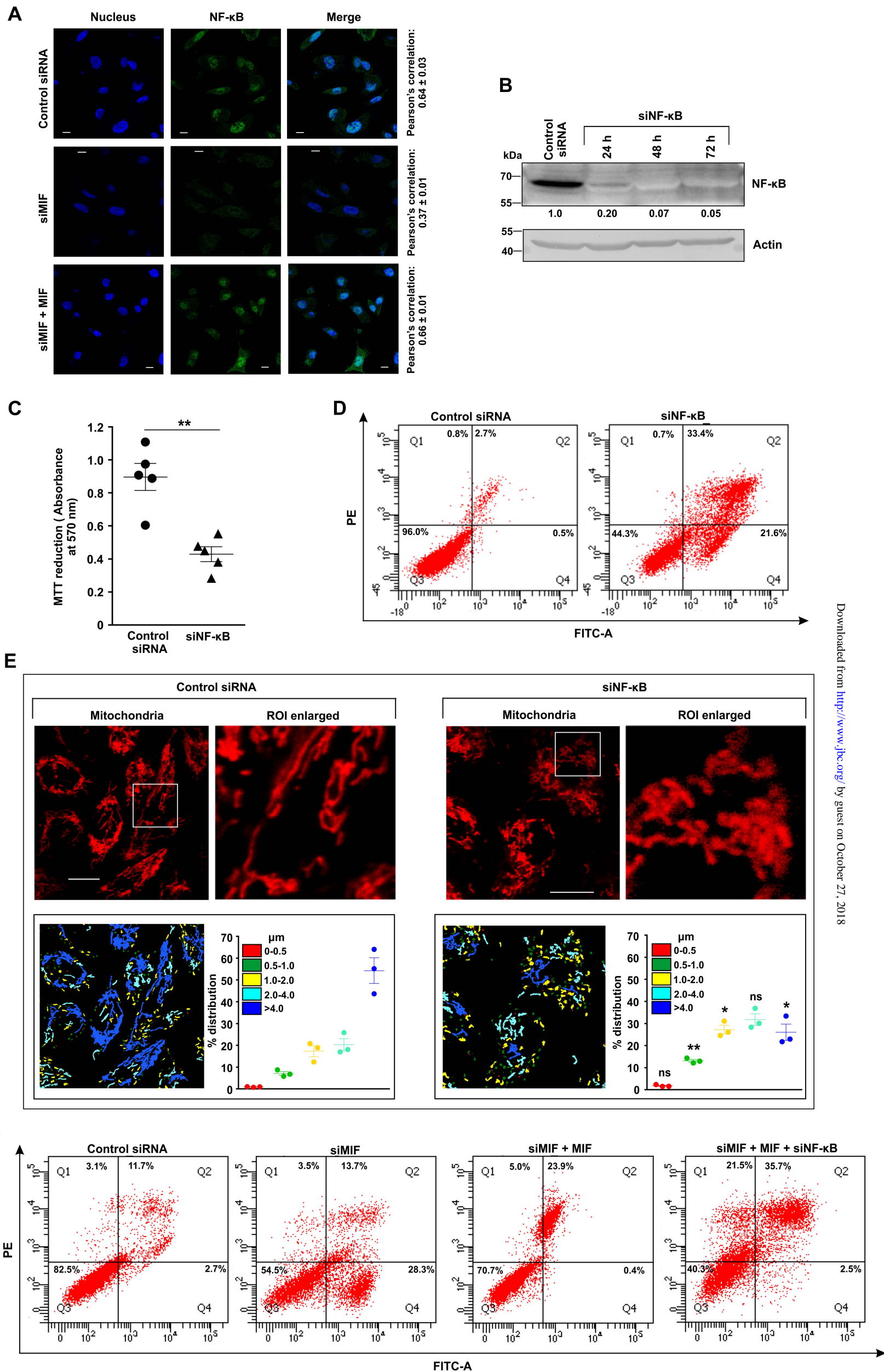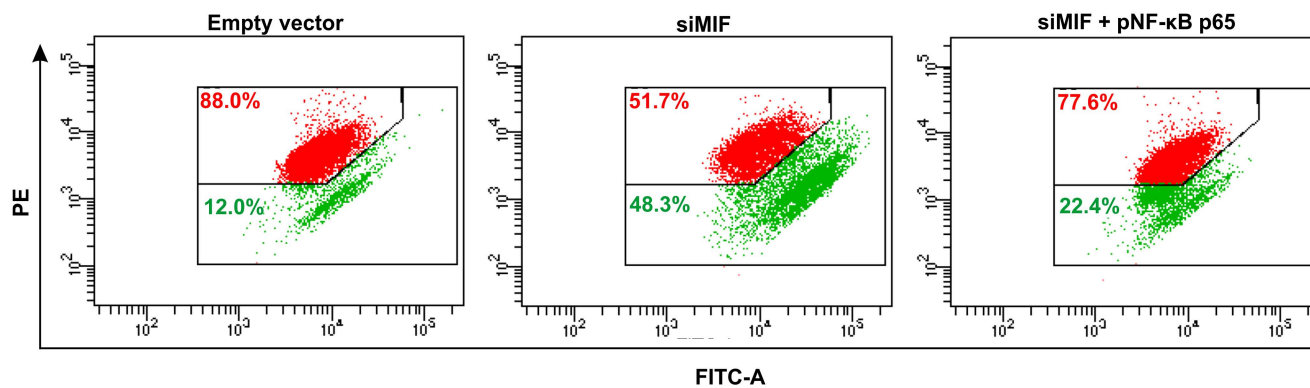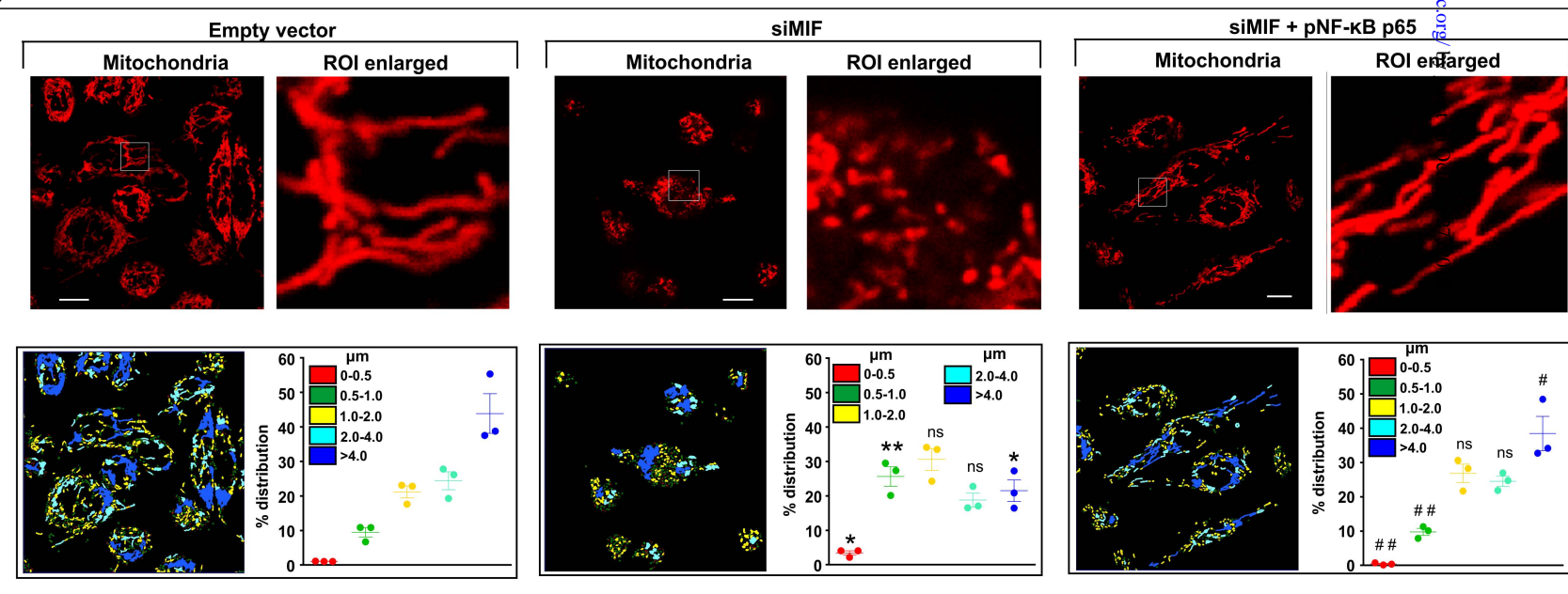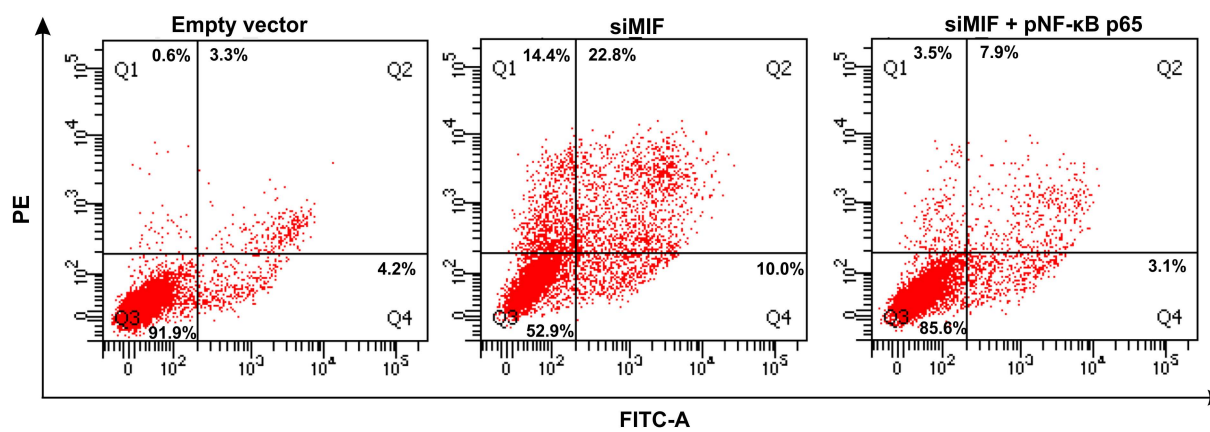
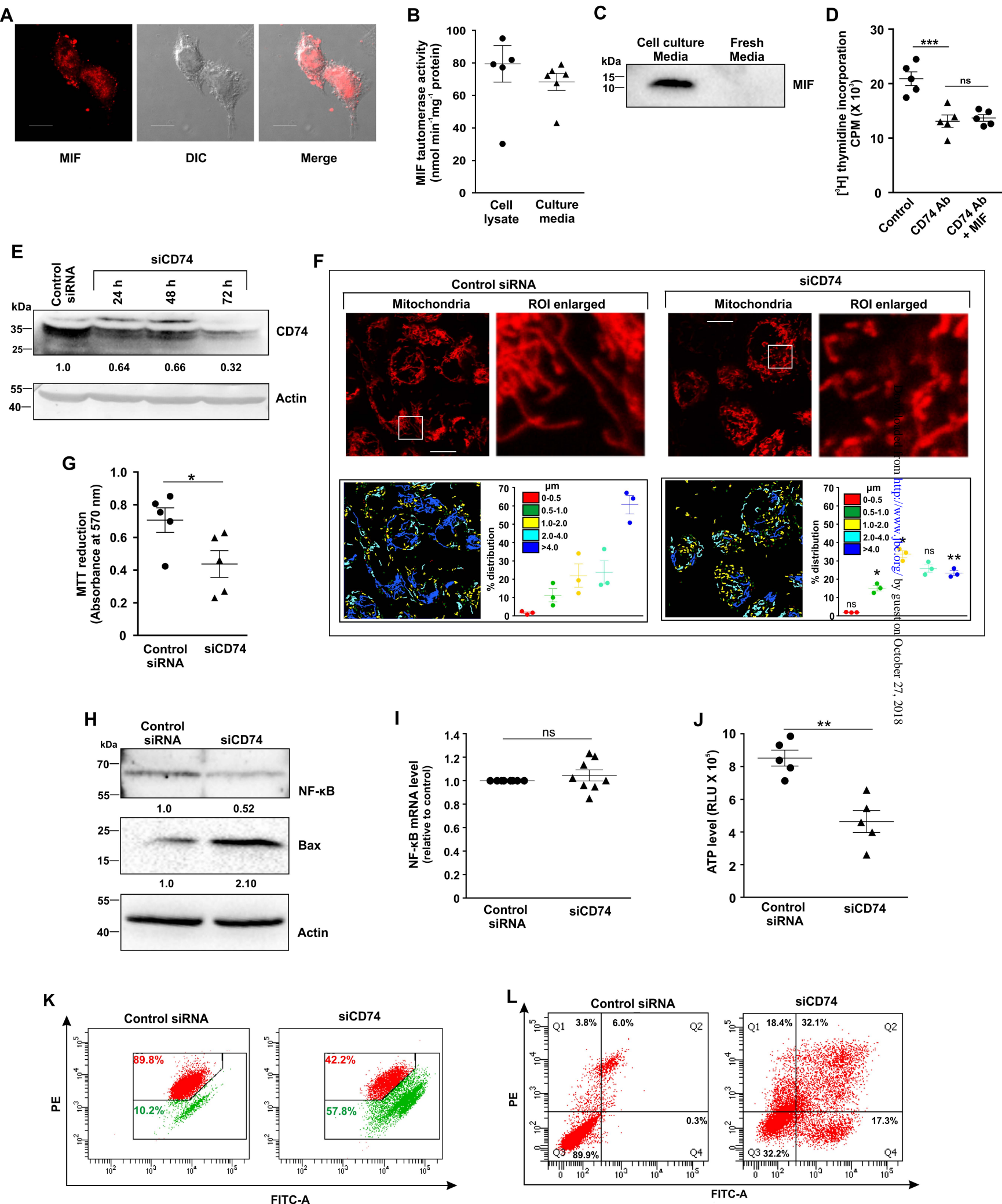# Figure 10

Figure 11

Macrophage migration inhibitory factor regulates mitochondrial dynamics and cell growth of human cancer cell lines through CD74-NF κB signaling

Rudranil De, Souvik Sarkar, Somnath Mazumder, Subhashis Debsharma, ASIM AZHAR SIDDIQUI, Shubhra Jyoti Saha, Chinmoy Banerjee, Shiladitya Nag, Debanjan Saha, Saikat Pramanik and Uday Bandyopadhyay

Access the most updated version of this article at doi: 10.1074/jbc.RA118.003935

Alerts:
- When this article is cited
- When a correction for this article is posted

Click here to choose from all of JBC's e-mail alerts